pss

+++rapid
research
letters +++

www.pss-rapid.com

Review@RRL

Growth and properties of InGaAs nanowires on silicon

Gregor Koblmüller[*, 1] and **Gerhard Abstreiter**[1, 2]

[1] Walter Schottky Institut, Physik Department, and Center of Nanotechnology and Nanomaterials,
 Technische Universität München, 85748 Garching, Germany
[2] Institute for Advanced Study, Technische Universität München, 85748 Garching, Germany

[*] Corresponding author: e-mail Gregor.Koblmueller@wsi.tum.de

Free-standing ternary InGaAs nanowires (NW) are at the core of intense investigations due to their integration capabilities on silicon (Si) for next-generation photovoltaics, integrated photonics, tunneling devices, and high-performance gate all-round III–V/Si NW transistors. In this review, recent progress on the growth, structural, optical and electrical properties of InGaAs NWs on Si substrate is highlighted. Particular focus is on a comparison between conventional catalyst-assisted and catalyst-free growth methods as well as self-assembled versus site-selectively grown NW arrays. It will be shown that catalyst-free, high-periodicity NW arrays with extremely high compositional uniformity are mandatory to allow un-ambiguous structure–property correlation measurements. Here, interesting insights into the electronic/optical properties of wurtzite, zincblende and mixed crystal phases of InGaAs will be highlighted based on recent photoluminescence spectroscopy data. Finally, the InGaAs NW-on-Si system is also discussed in the realms of heterojunction properties, providing a promising system for steep-slope tunneling field effect transistors in future low-power post-CMOS intergrated microelectronics and broad-band photoabsorption and detection devices.

1 Introduction III–V compound semiconductor nanowires (NW) are currently considered as the most versatile family of one-dimensional (1-D) nanostructures since they provide an enormous wealth for novel fundamental research as well as unique building blocks for various interesting applications. In particular, ternary InGaAs nanowires (NW) have fueled substantial interests due to recent advances in their integration on silicon (Si) and first demonstrations of prototype devices for next-generation photovoltaics [1], integrated photonics [2, 3], tunneling diode devices [4] and high-performance vertical gate all-round III–V/Si NW transistors [5]. The huge range of possible applications of the InGaAs NW system stems largely from its many unique properties. These are primarily the widely tunable band gap energies and emission wavelengths (~880–3500 nm), high electron mobilities, tunable Schottky barrier heights, and the overall reduced lattice

mismatch restrictions when integrated in its 1-D geometry on foreign substrates or as NW heterostructures. The latter should thus not only enable direct integration of InGaAs on Si – despite the huge lattice mismatch ($\Delta a/a = 4.2$–11.6% over the entire composition range) – but also the formation of low-defect density heterostructure devices that are not easily realized in conventional planar growth strategies. For instance, complex radial InGaAs–InP/InAlAs core–shell nanowire heterostructures were recently fabricated on Si and demonstrated to operate as high-mobility channels in vertical NW field effect transistors [5]. Likewise, the reduced lateral dimensions and, hence, much more effective strain relaxation of axial heterostructures opens several routes for integration and self-alignment of low-defect density GaAs/In(Ga)As-based NW heterostructures for applications in efficient single photon emission, bottom-up photonic crystal lasers, and quantum information processing [6, 7].

While various prototypical InGaAs NW-based device concepts have been elaborated, the fabrication/growth, optimization of InGaAs NW properties and improvement of device performance is all but trivial. This is mainly because much of the growth and optimization of InGaAs NW structures is still in its infancy and, as this review will point out, often strongly limited in compositional homogeneity and structural integrity as a natural consequence of alloying in ternary or multi-component material systems. Quite often, this makes it difficult to provide unambiguous data for fundamental intrinsic structure–property relationships, such as electronic band gap energy, and associated optical emission and electrical transport properties. In addition, various different growth modes can exist (e.g. vapor–liquid–solid growth, vapor-solid growth, self-assembled or site-selective growth, etc.) as well as a variety of different growth methods (metal-organic chemical vapor deposition (MOCVD), molecular beam epitaxy (MBE), etc.), which typically have different effects on the intrinsic NW properties complicating matters even more.

This review is therefore aiming at collecting, sorting and comparing the various available growth strategies for ternary InGaAs NW with respect to compositional homogeneity, structural integrity and resultant intrinsic electronic properties. In logical order, we will first describe the rather conventional catalyst-assisted growth approaches, followed by catalyst-free growth methods where we will also distiguish between self-assembled and site-selective (i.e., position-controlled) growth of InGaAs NW. Emphasis will be placed particularly on the determination of important intrinsic electronic properties of InGaAs NWs, such as band gap energy as derived from photoluminescence. We then also address the crucial aspects of strain relaxa-tion, defect formation and defect minimiza-tion at the InGaAs/Si heterointerface. Finally, the InGaAs-NW-on-Si hetero-interface will be highlighted as an interesting and promising system for functional heterojunction devices, in particular for tunneling diodes and associated tunneling field effect transistors.

Gregor Koblmüller is a principal scientist and lecturer at the Walter Schottky Institut and Physics Department at Technical University Munich (TUM). He received his doctoral degree in technical physics from the Vienna University of Technology in 2005, and worked as a graduate student researcher at Infineon Technologies, Corporate Research. He previously was a postdoctoral researcher and project scientist at the Materials Department at the University of California, Santa Barbara (UCSB) from 2005–2008. He is the recipient of the Young Investigator MBE Award in 2010. His research activities include semiconductor nanostructures, nanoelectronic and nanophotonic devices, wide band-gap materials (group-III nitrides), molecular beam epitaxy growth and nanoscopic metrology.

Gerhard Abstreiter is a professor at the Physics Department of the Technical University Munich (TUM) since 1987. He received his doctoral degree in Physics from the Physics Department at TUM in 1975, and worked subsequently at the Max-Planck-Institute for Solid-State Research in Stuttgart and Grenoble and the Physics Department at TUM. He served as director of both the Walter Schottky Institut and Center for Nanotechnology and Nanomaterials since their inception. He has been also a guest professor at various universities, including UC Santa Barbara, Columbia University (New York) and The University of Tokyo. He is the recipient of numerous awards, such as the prestigious Walter-Schottky Prize, the Gottfried-Wilhelm-Leibniz Prize, the Max Born Prize, the von Schelling Prize, and most recently the Stern-Gerlach medal. Currently, he is acting director of the Institute for Advanced Study (IAS) at TUM. His research interest covers experimental semiconductor physics with special emphasis to structural, electronic and optical properties of nanostructures, molecular beam epitaxy for high purity hetero- and nanostructures, self-assembly and self-organisation of semiconductor quantum dots, and development of novel devices for nano-electronics, opto-electronics, quantum information technology, and biosensing.

2 Growth of InGaAs nanowires

2.1 Gold (Au) catalyst-assisted vapor–liquid–solid (VLS) growth Among all fabrication processes catalyst-assisted growth has certainly become the most widespread method for the growth of free-standing III–V compound semiconductor NWs over the last few decades [8–12]. This is mainly a consequence of the very early successes in achieving highly anisotropic (i.e., high-aspect ratio) growth of whiskers when foreign catalysts are employed [13]. Typically, as foreign catalysts gold (Au) nanoparticles are used to form a liquid alloy droplet with the reaction species supplied by the surrounding vapor, leading to subsequent super-saturation and precipitation at the solid/liquid interface that triggers whisker (nanowire) growth in the so-called vapor–liquid–solid (VLS) growth mechanism [13]. While this VLS-type growth method was pioneered for the growth of high-aspect-ratio Si nanowhiskers, it was rather easily adapted also for the growth of other elemental or binary III–V semiconductor NWs. In particular, Au-catalyzed growth of both InAs and GaAs NWs has now been quite well established, where critical relationships between the size of the Au droplet, selected growth parameters and the growth kinetics have been elaborated for a variety of growth techniques [14–21].

In contrast, growth of Au-catalyzed ternary InGaAs NWs has proven not to be as straightforward, since the individual group-III elemental species underlie quite different properties in their surface diffusion, solubility and incorporation kinetics [22]. This was demonstrated extensively in the early work by Kim et al. [22], where In-rich InGaAs NWs were grown on GaAs (111)B substrates in a Au-catalyzed VLS method using MOCVD. It was found that at the selected growth temperature (450 °C) the

Review

@ RRL

Phys. Status Solidi RRL **8**, No. 1 (2014)
13

InGaAs NWs resulted in strong tapering and NW height distribution depending on the NW density. Strong NW tapering and non-uniform morphologies were also observed by Regolin et al., using similar growth processes [23]. Kim et al. explained the significant density and shape dependence by the large differences in surface diffusion of the respective In and Ga adatoms on the GaAs(111)B surface, with In adatom migration lengths being much longer than those of Ga adatoms. In fact, the non-uniform geometry of the NWs was further associated with a large In/Ga compositional variation along the NW, exhibiting three times higher In content near the base as compared to the tip region of the NWs as verified by energy-dispersive X-ray spectroscopy (EDX) and high-resolution transmission electron microscopy (TEM) [22]. Based on this it has been suggested that in VLS-growth of InGaAs NWs the species with higher diffusivity (In adatoms) generate an unintentional In-rich shell structure near the bottom of the NW that is responsible for the compositional nonuniformity [22, 24], which has been also explained by recent theoretical transient growth models [25]. In addition, In has a higher affinity for the Au catalyst than Ga [26–29], which is expected to further modify the composition of ternary InGaAs NWs during VLS growth. Indeed, Guo, et al. recently observed that due to this competitive solubility of In versus Ga adatoms, Au catalysts preferentially transport Ga to the NW growth front, resulting in a segregation of a Ga-rich (In)GaAs core region (via VLS-mode) and an In-rich InGaAs shell layer (via vapor-solid, VS-mode) [30]. Indium, on the other hand, remains rather in the Au–In alloy droplet and is only slowly incorporated at the liquid-solid interface underneath. This has also substantial consequences on the formation of e.g. axial NW heterostructures of GaAs/In(Ga)As, where it has been found that the GaAs/InAs interface is not sharp but contains an InGaAs transition segment of graded composition [31].

To summarize all these observations reported by the several groups [22, 24, 25, 30, 32], Fig. 1(a) depicts a schematic illustration of the growth model and resultant non-uniform composition distribution of InGaAs NWs as obtained by the Au-catalyzed growth mode. This schematic shows that besides a predominant Ga-rich VLS-type growth in the axial direction, mediated by the preferential precipitation of Ga atoms over In atoms as supplied primarily by surface diffusion fluxes, also an In-rich InGaAs shell layer evolves at the sidewalls in a VS-type growth mode.

In order to improve the compositional homogeneity in Au-catalyzed InGaAs NWs modified growth conditions were suggested which reduce the NW tapering and improve morphological homogeneity. Recent reports by Joyce et al. [24] and Shin et al. [32] indicate that reducing the growth temperature and V/III ratio in an MOCVD environment may reduce NW tapering, producing nearly straight InGaAs NWs over a length of several μm with reduced compositional variation [32]. Moreover, recent two-step InGaAs NW growth (high-temperature nucleation,

subsequent low-temperature growth) by CVD [33] and single-step growth of InGaAs NWs by thermal evaporation methods [34] reported also relatively straight NWs with decent compositional uniformity, although in these reports the NWs do not appear to grow in an epitaxial manner on the respective Si substrates.

2.2 Self-catalyzed vapor–liquid–solid (VLS) growth Besides the discussed difficulties in producing homogeneous InGaAs NWs via Au-catalyzed growth methods, the increasing efforts to integrate InGaAs NWs on Si substrate have posed various other limits to the use of Au catalysts. The main limitations are that Au causes deep level traps in Si [35], but also that Au may be incorporated into the NW [36]. In addition, the use of Au catalysts may trigger inclined growth due to exposure of all available ⟨111⟩-oriented facets on Si(111) [12, 37], while the high solubility of Si in Au [38] could even cause migration of Si into the Au droplet and hence unintentional Si doping of the III–V NWs.

In this sense, Au-free growth of NWs is much desired which can be realized by replacing the extrinsic Au catalyst droplet by an intrinsic droplet of the respective group-III element forming during the nucleation procedure. This so-called self-catalyzed (autocatalytic) growth of group-III arsenide-based NWs, which was originally pioneered on GaAs and InAs(111)B substrates [39–42], has nowadays become a very successful growth mode for GaAs NWs on Si(111) [43–49] predominantly achieved by MBE growth. Quite remarkable, while for self-catalyzed GaAs NWs the existence and role of the Ga droplet have been unambiguously veryfied, for InAs NW growth on Si(111) the existence of In droplets were never directly observed [50, 56]. Only very recently, Grap et al. [57] reported a self-catalyzed growth mode of In-assisted InAs NWs, however, yet on GaAs (111)B substrates. It has therefore remained questionable whether InAs NWs or In-rich InGaAs NWs can be grown on Si(111) via an In-droplet assisted growth mode.

Self-catalyzed VLS growth of InGaAs NWs as reported so far has therefore mainly taken place via the in situ formation and stabilization of Ga-rich droplets [58, 59]. Heiß et al. have shown that by adding In to the Ga-droplet there is a significant time delay for the In to precipitate underneath the alloy droplet, complicating the formation of sharp composition-tuned NW heterostructures [58]. Also, under the given growth conditions the incorporation of In was limited to less than 5%, i.e. $x(\text{In}) < 0.05$ [58]. In another growth temperature dependent study by Heiß et al. [59] (also performed on GaAs(111)B substrates) it was found that even by lowering the growth temperature the In concentration does not exceed 5% in the bulk of the InGaAs NW but rather forms an In-rich shell structure. The limited precipitation of In atoms and the formation of an In-rich shell structure resemble therefore closely the anticipated growth model of Au-catalyzed InGaAs NWs as presented in Fig. 1(a).
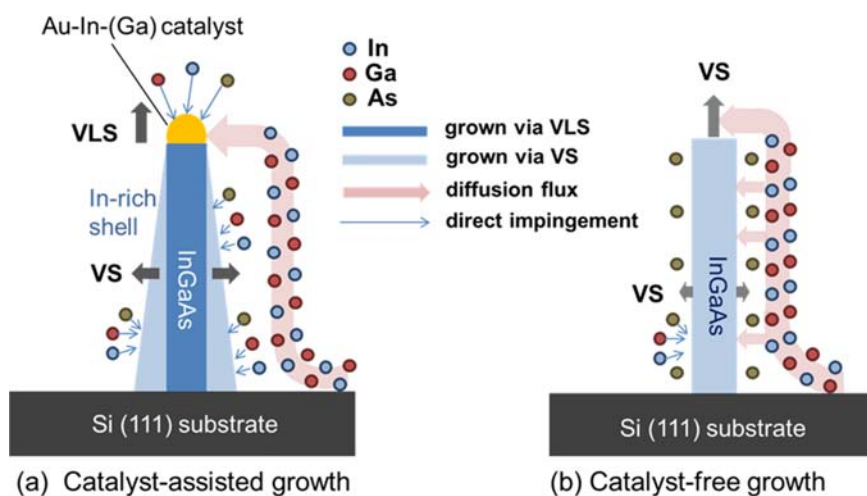
Figure 1 Schematic illustrations of (a) Au-catalyst assisted growth of InGaAs NWs which commonly results in a VLS-type axial growth of a preferrential Ga-rich InGaAs core and a VS-grown In-rich shell layer around, and (b) catalyst-free VS-type growth mode which produces typically higher compositional uniformity of InGaAs NWs. This growth mode is achieved mainly via the high anisotropies in growth rates of different facets, i.e., much higher growth rate along the axial [111] facet than compared to the {110} sidewall facets.

2.3 Catalyst-free vapor–solid (VS) growth Obviously, VLS-type growth of ternary InGaAs NWs and associated NW heterostructures – either by a foreign (Au) or a self-catalyst – is not an easy endeavor hampered by morphological instabilities (NW tapering and bowing), significant compositional inhomogeneity, large dispersion in the incorporation ratio of the supplied group-III atoms (i.e., limited indium incorporation) and non-abrupt axial material boundaries. In this respect, a growth mode which is completely free of metallic droplet catalysts might be more favorable for producing InGaAs NWs of desired morphological and compositional uniformity.

Recently, various different strategies for catalyst-free InGaAs NWs grown in the VS growth mode were suggested: One relatively simple approach is to use mechanically roughened Si substrates to produce catalyst-free, self-assembled InGaAs nanoneedles (NNs) by MOCVD as demonstrated by Moewe et al. (i.e., "nanoneedle" or "nanocone" growth mode) [3]. Under the given low-temperature (400–420 °C) growth conditions the obtained NNs showed significant tapering (very large base diameters up to ~600 nm, ~2–5-nm-thin NN tip), while the NNs became shorter upon increasing the In composition from $x(\text{In}) = 0$ to 0.15. In a follow-up work, the same group elucidated the underlying growth mechanism that leads to the complex NN-shaped InGaAs structures [60]. Essentially, during the nucleation of InGaAs islands directly on Si a parasitic polycrystalline InGaAs layer forms with a slow growth rate around the bottom of these islands, resulting first in a highly defected inverted InGaAs cone structure before the actual NN growth resumes with a high WZ-phase purity toward the tip region. Here, the authors also observed significant length saturation with increasing growth time and In composition, which they attributed to a sudden crystal phase switch from WZ to a few-ML-thin

ZB layer at the growth front terminating growth in the axial direction [60]. This observation coincided also with a significantly larger In content at the NN tip as compared to the base, suggesting a non-uniform In distribution along the axis of the NNs. Remarkably, from these InGaAs NNs operating nanolasers and InGaAs/GaAs QW light emitting diodes could be fabricated [61, 62].

Catalyst-free, self-assembled InGaAs nanorods and NWs grown in a completely mask-less and droplet-free mode have been also reported by a few other groups. Shin et al. [1] demonstrated that morphologically relatively uniform, non-tapered and high-aspect ratio InGaAs NWs could be spontaneously grown on Si substrate over almost the entire compositional range, $x(\text{In}) = 0.2 - 1$, using MOCVD. Interestingly, the NW diameter was found to be inversely proportional to the lattice mismatch (as governed by the In composition) and was further tunable by the MOCVD growth conditions. In a more recent work, Shin et al. [63] identified that small compositional fluctuations occurring intermittently for a few MLs produce non-uniform strain across the NWs which may cause them to bend. However, the overall compositional uniformity of In and Ga is quite homogeneous along the entire length and cross-section of the InGaAs NWs [63], in strong contrast to what is commonly found for catalyst-assisted VLS-grown InGaAs NWs (compare Fig. 1(a)) [22–24, 30, 32, 59]. The homogeneous incorporation of growth species in the catalyst-free, VS-type growth mode is schematically also illustrated in Fig. 1(b). In the VS growth mode the axial growth rate is typically much lower than in the VLS growth mode [48], and growth is mainly governed by the high anisotropies in the growth rates of different facets, i.e., much higher growth rate along the axial [111] facet than compared to the {110} sidewall facets. The shape and morphology of the NW hence follows conventional

Phys. Status Solidi RRL **8**, No. 1 (2014)

15

Wulff's construction theory [64], stating that the slowest growing surface ({110}-sidewalls) will appear as the largest developed facet. Such growth anisotropies, however, are governed by the specific surface energies of the respective facets, which are very sensitive on the chemical potential μ, and therefore strongly governed by growth conditions. These facet-dependent growth anisotropies describe thus the underlying mechanism for catalyst-free VS-type growth of NWs, independent of whether they are grown either directly on a foreign substrate such as Si (hetero-epitaxy) or on any given substrate (including homoepitaxy) as in the case of selective area growth (SAG) as discussed below. Nevertheless, despite the good morphological/compositional homogeneity achieved in individual VS-grown InGaAs NWs by Shin et al. [63], measurements of the entire NW ensemble revealed that these were much more inhomogeneous as a result of the self-assembled growth mode. This yielded not only large dispersion in NW length and diameter but also significant InGaAs composition fluctuations over the whole ensemble, as verified by the relatively broad linewidths in PL and 2θ–ω high-resolution XRD spectra [1].

Obviously, one of the most promising approaches for ultimate composition control over large InGaAs NW ensembles is considered to be site-selective growth of periodic arrays. Such growth of periodic InGaAs NW arrays is most conveniently achieved by use of pre-patterned masks (such as SiO$_2$) for selective area growth (SAG), as demonstrated in various recent MOCVD growth experiments by researchers from Hokkaido University [5, 65–69]. Utilizing thin SiO$_2$ mask layers with openings fabricated by electron beam lithography (EBL) and subsequent etching, SAG of high-periodicity and high-homogeneity InGaAs NWs was thus achieved on different substrates, such as e.g. InP(111)B [65–68], Si(111) [5], and GaAs(111)B [69]. All these reports elaborated complex dependencies of the NW growth rate on various different parameters, such as MOCVD growth conditions (V/III ratio, growth temperature), mask opening diameter and NW density (i.e., mask pitch). Insights into the nucleation and growth mechanism were also gained, showing that during the first stages of growth the NW diameters were roughly matching with the opening mask diameter while the height of the NWs increased super-linearly with time [65]. In contrast, for longer growth times both the NW diameter and length increased rather linearly with time, suggesting steady-state growth [65].

2.3.1 Comparison of self-assembled and site-selective InGaAs NW growth While much of the morphological details in site-selective growth of InGaAs NWs have been studied, less attention has been paid to measurements of their compositional uniformity. In the following, we provide a direct comparison of the compositional homogeneity in site-selective NWs with that of self-assembled NWs grown in the catalyst-free VS-type growth mode, particularly for InGaAs NWs with high-to-inter-

mediate In-content. SiO$_2$-coated Si(111) wafers were used as substrates, which were processed either by nanoimprint lithography (NIL) to serve as templates for site-selective growth or by simple wet chemical etching (i.e., *non-lithographically*) in buffered hydrofluoric (HF) acid to generate random nucleation sites for self-assembled growth. In the first case, ~20-nm-thick thermally grown SiO$_2$ was employed, while in the latter case rf sputter-deposited SiO$_x$ was used that was etched back to a final oxide thickness of ~2–5 nm [70]. Further details on the template preparation can be found elsewhere [70–72]. All respective InGaAs NW growth experiments were performed by solid-source MBE under highly As-rich growth conditions (As/(Ga + In) flux ratio = 56.5) at a fixed growth temperature and growth time of $T = 550$ °C and $t = 1$ h (or 24 min), respectively. These growth conditions appear quite different to what is commonly used for high In-content In(Ga)As NW growth by MBE, however, these conditions and access to high-T growth were found essential to enable sufficiently high Ga diffusion and incorporation into (111)-oriented InGaAs NWs [73]. In order to tune the composition of the InGaAs NWs, we adjusted the ratio between the Ga and In flux, i.e., ($\phi^{Ga}/\phi^{In} + \phi^{Ga}$), while keeping the total group-III flux constant.

A typical example for a site-selective NW growth experiment on NIL-patterned SiO$_2$/Si(111) templates is illustrated in Fig. 2 for a growth run with ($\phi^{Ga}/\phi^{In} + \phi^{Ga}$) = 0.1. The photograph on the lower right shows clearly the region of NW growth (in black) as delineated by the ~1 × 1 cm^2 large imprint stamp employed at the center of the 2-inch Si(111) wafer. This result demonstrates the excellent NIL fabrication and selective InGaAs NW growth, since the surrounding unpatterned SiO$_2$ area (in grey) appears completely specular. The upper right-hand and left-hand images show sectional top-view and side-view scanning elec-
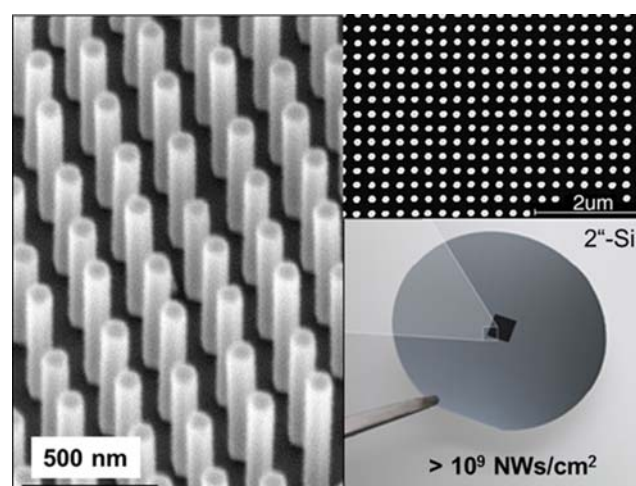
Figure 2 Typical example of site-selective growth of InGaAs NWs on NIL-patterned SiO$_2$/Si(111) substrates ($\phi^{Ga}/\phi^{In} + \phi^{Ga}$ ratio = 0.1), showing a full photograph of the as-grown 2-inch wafer (lower right) and the corresponding top-view (upper right) and side-view (left) SEM images.
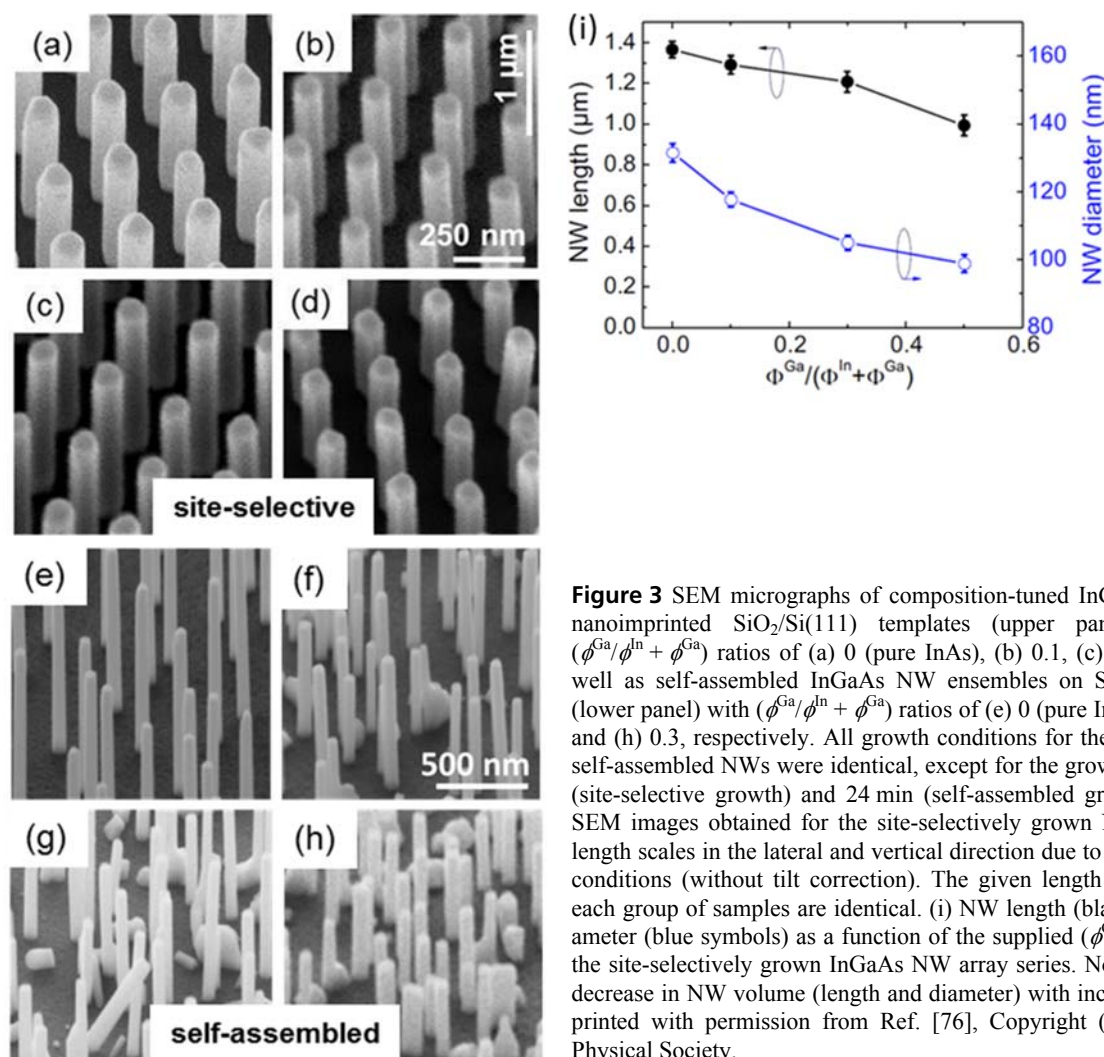
Figure 3 SEM micrographs of composition-tuned InGaAs NW arrays on nanoimprinted SiO$_2$/Si(111) templates (upper panel) with different ($\phi^{Ga}/\phi^{In} + \phi^{Ga}$) ratios of (a) 0 (pure InAs), (b) 0.1, (c) 0.3, (d) and 0.5; as well as self-assembled InGaAs NW ensembles on SiO$_x$-masked Si(111) (lower panel) with ($\phi^{Ga}/\phi^{In} + \phi^{Ga}$) ratios of (e) 0 (pure InAs), (f) 0.1, (g) 0.2, and (h) 0.3, respectively. All growth conditions for the site-selectively and self-assembled NWs were identical, except for the growth time, i.e., 60 min (site-selective growth) and 24 min (self-assembled growth). Note that all SEM images obtained for the site-selectively grown NWs show different length scales in the lateral and vertical direction due to the specific imaging conditions (without tilt correction). The given length scales given within each group of samples are identical. (i) NW length (black symbols) and diameter (blue symbols) as a function of the supplied ($\phi^{Ga}/\phi^{In} + \phi^{Ga}$) ratio for the site-selectively grown InGaAs NW array series. Note the characteristic decrease in NW volume (length and diameter) with increasing Ga flux. Reprinted with permission from Ref. [76], Copyright (2013) by American Physical Society.

tron micrograph (SEM) images of the same InGaAs NW array, indicating the excellent periodicity and very high vertical, i.e., (111)-oriented growth yield of >90% (growth yield refers to vertically aligned NWs/mask opening) [71]. The selected pitch of the NIL stamp (250 nm with 60 nm hole diameter) along with the high growth yield correspond to a homogeneous NW density of ~2.5 × 10^9 NWs within the ~1 × 1 cm^2 imprinted area. The fabrication of such large-area, high-density NW arrays are a major advantage of the employed NIL-method, due to its very time-efficient processing characteristics in comparison with other conventional lithography-based techniques (e.g. electron beam lithography which takes ~100× longer to fabricate the same-size pre-patterned substrate [70]).

Figure 3 compares typical morphologies of site-selectively grown InGaAs NW arrays (a–d) and self-assembled InGaAs NW ensembles (e–h) on SiO$_2$-coated Si(111), as obtained by SEM. The group-III flux ratio for these two exemplary sample series was varied between ($\phi^{Ga}/\phi^{In} + \phi^{Ga}$) = 0–0.5, corresponding to a tunable InGaAs composition with Ga contents of up to x(Ga) = 0.36 as

determined by XRD and energy-dispersive X-ray spectroscopy (EDXS) (see below). Similar to Fig. 2, all SAG-InGaAs NW samples show excellent growth selectivity over large imprinted areas [71]. The perfect alignment of the NWs along the (111)-orientation holds true also for all the investigated flux ratios (InGaAs compositions) and further confirms the direct epitaxial relationship with the underlying Si(111) substrate [52, 53]. In addition, the homogeneity in NW length and diameter is quite high with very low deviations from the average values as expected from the highly periodic growth.

In contrast, the self-assembled InGaAs NWs (lower panel of Fig. 3) show spatially a very random distribution of NWs, given by the statistical distribution of the nucleation sites that are created by HF-etched pinholes in the thin SiO$_x$ layer [52, 53, 73]. Despite the fact that on average the NW densities were comparable between the site-selective and self-assembled NW (ρ^{NW} ~ 2.5 × 10^9 cm^{-2}), the variation in the nearest-neighbor distance for the latter ranged from ~150 nm to ~400 nm. This range represents a length scale regime where under the given growth conditions the

Table 1 Average length (L) and diameter (D) as well as corresponding standard deviation of InGaAs NWs grown under different ($\phi^{Ga}/\phi^{In} + \phi^{Ga}$) ratios, as derived from statistical analysis of >10 NWs/sample using SEM. The data compares site-selectively grown NWs on NIL-SiO$_2$/Si(111) templates (growth time: 60 min) with self-assembled NWs on non-lithographically prepared SiO$_x$/Si(111) (growth time: 24 min). Also shown are the XRD-measured Ga content x(Ga) and FWHM of the InGaAs-related 2θ-peak reflection as extracted from 2θ–ω scans performed with beam size of ~3×4 mm^2 and a 1/8° aperture at the detector. Data labeled with an asterisk (*) refers to the NW-based signature in the 2θ–ω scan of Fig. 3a as derived from peak fitting analysis (Voigt function). Reprinted with permission from Ref. [71], Copyright (2012) by American Physical Society.

| growth type	$\phi^{Ga}/\phi^{In} + \phi^{Ga}$	L (nm)	D (nm)	x(Ga) [XRD]	2θ-FWHM (°)
SAG	0	1365 ± 40	131 ± 2.7	0	0.031
	0.1	1290 ± 44	118 ± 2.2	0.07	0.031
	0.3	1207 ± 50	105 ± 2.1	0.19	0.039
	0.5	993 ± 50	99 ± 2.6	0.36	0.039*
Self assembly	0	860 ± 88	83 ± 7	0	0.031
	0.1	645 ± 124	65 ± 7	0.08	0.084
	0.2	681 ± 68	81 ± 5	0.15	0.084
	0.3	423 ± 80	73 ± 9	0.19	0.091

collection and redistribution of group-III adatoms by neighboring NWs is strongly competitive [72]. Hence, any deviation in the interwire distance will inevitably lead to fluctuations in NW length and diameter and likely also in composition in the NW ensemble. It is obvious from Fig. 3(e–h) that closer spaced NWs are shorter and narrower than wider spaced NWs, giving the overall significant fluctuations in NW length and diameter as a result of the self-assembled process as also seen by Shin et al. [1, 63]. These details are also summarized in Table 1, indicating that the standard deviation in NW length and diameter is ~2× higher for self-assembled NWs although their total lengths were grown to approximately only half the length of the site-selective NWs. Furthermore, it is important to point out that independent of the type of growth (self-assembled versus site-selective) the as-grown NWs evidence a completely non-tapered morphology independent of the supplied ($\phi^{Ga}/\phi^{In} + \phi^{Ga}$) ratio. This fact along with the absence of any group-III elemental droplet (self-catalyst) on top of the NWs confirms that the catalyst-free InGaAs NW growth is governed by a clear VS-type growth mechanism, as has been also verified by the abrupt droplet-free nucleation characteristics in recent *in-situ* reflection high electron energy diffraction (RHEED) experiments [53]. Further details on the nucleation and growth mechanism may be obtained by investigating the NW tip morphology more closely. From the SEM images in Fig. 3 it appears that the morphology of the NW tip is not composed of a symmetric hexagonal surface layer, but rather resembles a tetrahedral shape. This type of tip morphology has been commonly observed in non-catalytically grown GaAs-based NWs by selective area epitaxy, and was associated with the nature of the NW nucleation mechanism. In particular, Ikejiri et al. (Ref. [74]) and Yoshida et al. (Ref. [75]) pointed out that tetrahedral GaAs islands grow at an early stage of growth, since these are energeti-

cally more favorable over hexagon-shaped islands. When growth proceeds, however, rotational twins and stacking defects are introduced which cause a change in shape from tetrahedral islands to hexagon-shaped NWs. Indeed, as further shown below in Section 3 the investigated InGaAs NWs contain a large number of stacking defects. Therefore, for non-catalytically grown VS-type NWs twins and stacking defects play an important role in stabilizing hexagon-shaped NWs, such that one can consider the underlying growth mode as a twin- and stacking-defect induced mode.

Further insights into the growth kinetics are gained from close investigation of the ($\phi^{Ga}/\phi^{In} + \phi^{Ga}$)-ratio dependence on the resulting NW length and diameter. As shown in Fig. 3(i) for site-selectively grown InGaAs NWs increasing ($\phi^{Ga}/\phi^{In} + \phi^{Ga}$) ratio results in a decrease in NW length and also a slight decrease in diameter under otherwise fixed growth conditions. Very similar tendencies are also observed for self-assembled InGaAs NWs, as further evidenced in Table 1. There are a few reasons which can explain this overall decrease in NW volume; i.e., (a) competing growth of parasitic InGaAs clusters in-between NWs which, however, is only seen marginally for the highest investigated ($\phi^{Ga}/\phi^{In} + \phi^{Ga}$) ratio of 0.5, and (b) reduced diffusivity and hence lower incorporation probability of In adatoms in the presence of Ga. The latter is considered as the most likely rate limiting mechanism, since similar composition-dependent growth behavior has been also observed in MOCVD growth experiments [65, 66].

In order to evaluate the precise composition of the respective InGaAs NW arrays grown under the different ($\phi^{Ga}/\phi^{In} + \phi^{Ga}$) ratios, 2θ–ω XRD scans were performed and the Ga-content x(Ga) determined using Vegard's law assuming that the NWs are completely relaxed. As boundary conditions for Vegard's law we applied the as-measured peak reflections of InAs ($2\theta = 25.33°$) and GaAs ($2\theta = 27.30°$) from which the alloy composition was line-
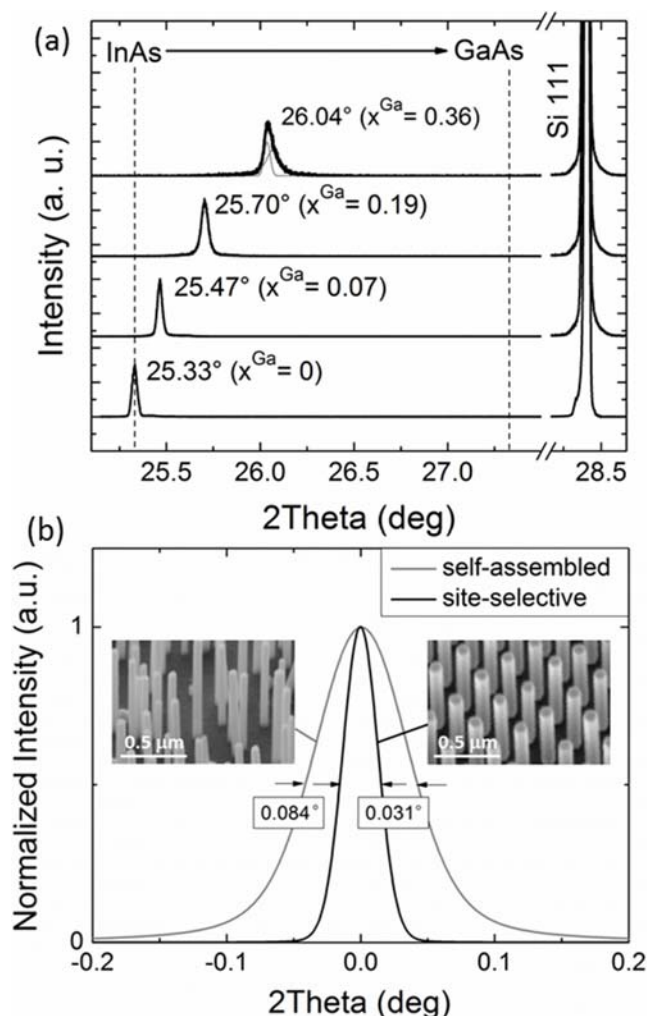
Figure 4 (a) XRD 2θ–ω scans of site-selectively grown InGaAs NW arrays on NIL-SiO$_2$/Si(111) grown under various different $(\phi^{Ga}/\phi^{In} + \phi^{Ga})$ ratios as given in Table 1. Dashed lines indicate the measured 2θ-peak positions of binary InAs and GaAs, allowing linear interpolation of the actual Ga content x(Ga) from the respective 2θ-peak positions of the InGaAs NW arrays via Vegard's law. The uppermost scan (x(Ga) = 0.36) shows two fitted curves in grey at $2\theta = 26.037°$ and $26.065°$, associated with wurtzite-based NW and zincblende-based cluster signatures, respectively (see also Ref. [71]). (b) Normalized intensity of the 2θ-InGaAs peak position (fixed at $2\theta = 0$) of site-selectively grown InGaAs NWs (x(Ga) = 0.07, black) and self-assembled InGaAs NWs (x(Ga) = 0.08, grey) grown with similar InGaAs composition. Insets illustrate typical SEM images of the two different types of NWs. Reprinted with permission from Ref. [71], Copyright (2012) by American Physical Society.

arly interpolated for the different InGaAs NW samples via shifts in 2θ peak position (and respective lattice constant). In Fig. 4(a) we show representative 2θ–ω XRD scans of site-selectively grown InGaAs NW arrays, normalized with respect to the peak intensity of binary InAs NWs and using an offset in intensity for better representation. It is obvious that besides the Si(111) substrate peak ($2\theta = 28.44°$) and

the composition-dependent InGaAs NW peaks no other reflections were observed over a 2θ–range of 0–60°. This confirms directly the perfect epitaxial relationship between the InGaAs NWs and Si, i.e., coherent orientation of InGaAs[111] || Si[111]. For the supplied $(\phi^{Ga}/\phi^{In} + \phi^{Ga})$ ratios of 0.1, 0.3 and 0.5 the corresponding 2θ-peak positions of the InGaAs NWs translate to Ga contents x(Ga) of 0.07, 0.19 and 0.36, respectively [71]. Note, that the XRD spectrum of the sample with x(Ga) = 0.36 shows an asymmetric shoulder at $2\theta = 26.065°$ related to the zincblende (111) reflection and which stems from parasitic clusters formed in between the NWs for this growth [71].

The Ga content x(Ga) as measured by XRD across the NW ensemble was also confirmed independently by chemical analysis of individual InGaAs NWs using EDXS. Figure 5(a) shows a TEM and scanning-TEM (STEM) micrograph along with (b) a corresponding line scan across the EDXS spectral map of a single InGaAs NW (taken from the site-selectively grown NW array sample with an XRD-measured Ga content of x(Ga) = 0.19). The line profiles for both Ga and In were found to be constant within experimental error from NW bottom to top. This demonstrates that the ternary composition of the respective InGaAs NWs is very uniform over the entire NW length, as expected from the catalyst-free VS growth mode. In addition, by extracting both the Ga fraction from the K lines
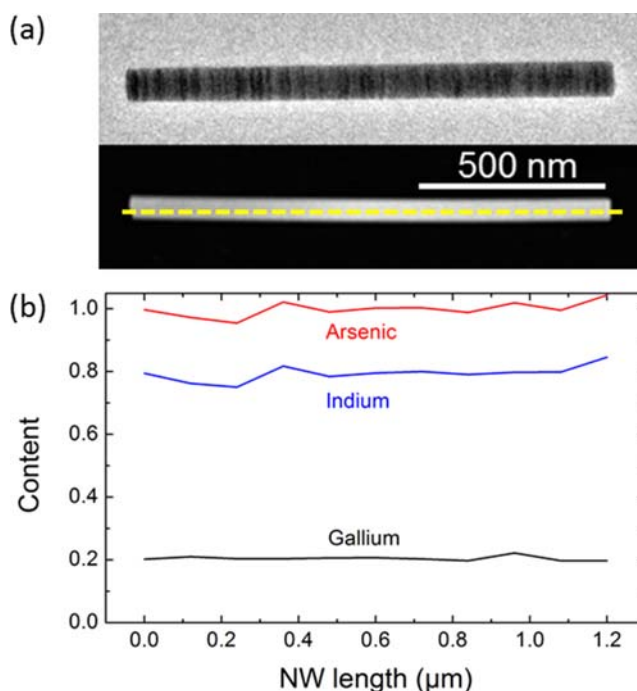
Figure 5 (a) TEM and STEM micrographs (top and center images) and corresponding EDXS line scan showing (b) the compositional profile across an individual InGaAs NW as taken from the site-selectively grown InGaAs NW array with an XRD-measured Ga content of x(Ga) = 0.19. The Ga content extracted from EDXS is x(Ga) = 0.2 ($\pm$0.02), in excellent agreement with the XRD-measured data.

Phys. Status Solidi RRL **8**, No. 1 (2014)

19

of Ga, In and As in the X-ray spectrum, we quantified the Ga content $x(Ga)$ to 0.2 (± 0.02 experimental error) in very good agreement with the XRD-measured data. In total, more than 5 NWs have been measured per sample, evidencing that the extracted Ga content was well within the experimental error of the measurements of a single NW. This indicates that the fluctuations in composition from NW to NW are very low and thus demonstrates very high compositional uniformity for the site-selectively grown NWs.

Concurrently, the compositional uniformity across the entire NW array can also be evaluated directly from the 2θ–ω XRD scans by measuring the full-width-at-half-maximum (FWHM) values of the respective InGaAs-NW related 2θ-peak reflection [71]. From the as-measured and subsequently fitted FWHM data (see also Ref. [71] for details), one finds that the FWHM values of the InGaAs-NW related 2θ-peak are all very similar, i.e., within the range of FWHM(2θ) = 0.031–0.039°, and do not deviate from the FWHM value obtained for binary InAs NWs. This evidences that the peak broadening is mainly limited by structural features and not by compositional inhomogeneities [71]. In contrast, much broader FWHM values were measured for the self-assembled InGaAs NW ensembles, as exemplified in Fig. 4(b) for InGaAs NWs grown under very similar conditions, i.e., yielding similar composition ($x(Ga)$ = 0.07–0.08). Obviously, the self-assembled NW ensemble shows a peak broadening that is more than a factor of 2 larger (FWHM = 0.084°) than the corresponding site-selectively grown NW array. However, the FWHM values of site-selective and self-assembled binary InAs NW arrays were completely identical (0.031°, see Table 1), suggesting that the significant peak broadening obtained for the self-assembled InGaAs NWs must be related to substantial compositional fluctuations across the NW ensemble. As Table 1 shows, the peak broadening is consistently observed also for all other self-assembled InGaAs NW samples, which is thus characteristic for the self-assembled process and its competitive diffusion and incorporation processes among NWs when different interwire distances are present. In other words, this means that due to the different diffusion lengths of Ga and In adatoms on the SiO$_2$ mask layer any variations in interwire distance will result in differences in the arrival and incorporation ratios between Ga and In species, hence causing InGaAs compositional variations across the ensemble of NWs.

Moreover, the larger compositional inhomogeneity in self-assembled InGaAs NWs has been also verified by micro-Raman spectroscopy measurements of the respective peak broadening of LO phonon modes [71].

**3 Structural properties of InGaAs nanowires** In order to describe the intricate relationship between growth, compositional uniformity and resulting microstructural properties of catalyst-free InGaAs NWs, we have performed systematic TEM analysis on individual NWs from the various sample sets and compare these with reported

literature data. All experimental details regarding the TEM analysis are described in Ref. [76], where diffraction patterns and high-resolution (HR) TEM images were recorded in a $\langle 110 \rangle$ zone axis geometry which corresponds to the side facets of the NWs. Data presented here are representative for each sample based on a statistical analysis of at least >5 NW/sample. Characteristic diffraction patterns and HR-TEM images of catalyst-free and site-selectively grown composition-tuned InGaAs NWs are shown in Fig. 6.

Interestingly, as opposed to the commonly observed bulk zincblende (ZB) crystal phase of InGaAs the as-grown NWs evidence a wurtzite (WZ)-dominated crystal phase. This is most clearly seen in the respective selective area diffraction (SAD) pattern of pure InAs NWs ($x(Ga)$ = 0, Fig. 6a). Here, the WZ phase is clearly defined by WZ sensitive reflections $1\bar{1}2$ and $\bar{1}12$ (as marked by arrows) occurring as distinct spots in the diffraction pattern. The diffraction pattern also evidences the existence of stacking faults (SFs) along the growth direction of the NW, indicated by the streaks in the SAD. The WZ-dominated crystal phase is further confirmed by the respective HR-TEM image recorded from the same NW (Fig. 6b). The micrograph shows individual WZ segments with short segment lengths (up to >10 nm) interrupted by stacking faults. On the other hand, no extended ZB segments could be observed along the entire length of the NW.

For ternary InGaAs NWs the intensities of the WZ sensitive reflections $1\bar{1}2$ and $\bar{1}12$ in the SAD patterns become gradually weaker upon increasing Ga content $x(Ga)$ and ultimately disappear when the highest investigated $x(Ga)$ was reached (see Fig. 6c–h). For the latter, only streaks are observed characteristic for heavily disordered layer stacking which could not be indexed by WZ reflections anymore. This trend is also noted in the respective HR-TEM images, indicating that the frequency of SFs increases while the average length of the WZ segments decreases towards larger Ga content. For $x(Ga)$ = 0.36, a completely random layer stacking is found where individual WZ segments are difficult to identify.

It is worth noting that such heavily faulted microstructure is quite common for catalyst-free (111)B-oriented In(Ga)As NWs grown in the VS-type growth mode [1, 5, 48, 77]. Particularly, under high As overpressure (high As/(Ga + In) ratio) stacking faults and twin defects can form quite readily on the (111)B growth plane [74, 75]. This fact is most likely related to the specific As-rich growth conditions, where it is well known that an As-rich (2 × 2) reconstructed (111)B surface structure is the energetically most favorable surface reconstruction [74, 78–81] that modifies the surface energies for preferential twin and stacking fault formation. In fact, recently a (2 × 2) reconstructed (111)B surface was even found to be a prerequisite for catalyst-free arsenide-based NW formation under As-rich conditions [75]. Like in planar growth of (111)B arsenide-based heterostructures [80, 81], it is therefore considered that very precise growth control with lower As
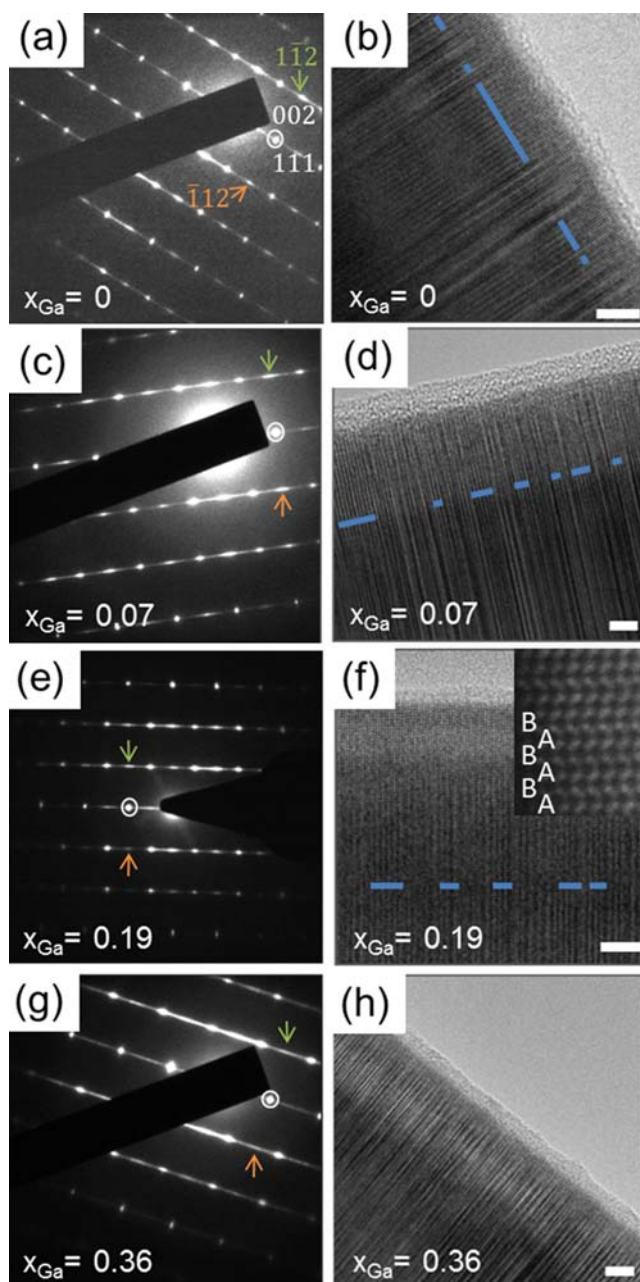
Figure 6 Diffraction patterns and corresponding HR-TEM images of site-selectively grown InGaAs NWs with different Ga-contents of (a), (b) x(Ga) = 0 (pure InAs), (c), (d) x(Ga) = 0.07, (e), (f) x(Ga) = 0.19, and (g), (h) x(Ga) = 0.36. WZ sensitive reflections $1\bar{1}2$ and $\bar{1}12$ are marked by arrows and are observed in all diffraction patterns, except for the InGaAs NW with highest Ga-content (x(Ga) = 0.36). Streaks parallel to the growth directions reveal an underlying disordered structure with stacking faults. The HR-TEM images evidence the individual layer stacking of each sample, with WZ segments marked in blue. The inset in (f) is a sectional STEM image of the same NW, illustrating the predominant hexagonal AB stacking sequence. The scale bar for all HR-TEM images is 5 nm. Reprinted with permission from Ref. [76], Copyright (2013) by American Physical Society.

overpressure is required to achieve defect-free (111)B-oriented InGaAs NWs in the catalyst-free VS-type growth regime.

Despite the high density of defects, the dominant crystal phase found in the present In-rich InGaAs NWs is WZ phase. This is quite interesting, because in most cases of group-III arsenide NWs the WZ phase stabilizes only for very thin NWs (with diameters of few tens of nm), whereas the NWs investigated here have relatively large diameters (>100 nm). WZ-phase InGaAs NWs were recently also found in the catalyst-free "nanoneedle (nanocone)" growth mode, where NW diameters were even significantly larger [60]. This is in contrast to observations of In-rich InGaAs NWs by Shin et al. [1, 63], although growth took also place in a catalyst-free, self-assembled manner on Si with NW diameters comparable to those presented here. In their work the dominant crystal phase for In-rich InGaAs NWs was found to be ZB [1], however, they also noted a higher degree of crystal phase disorder when increasing the Ga content to intermediate composition ranges similar to our case [63]. Twinned ZB superlattice structures and crystal phase mixing (alternating ZB and WZ phases) were also reported for catalyst-assisted (Au-catalyzed) InGaAs NWs grown from InAs and GaAs powders [34]. Surprisingly, similar catalyst-assisted VLS-type growth from powders reported, however, phase-pure ZB microstructure (independent of Ga content) despite the fact that the obtained NWs were extremely thin (diameter <20 nm) [33, 82].

Given these various findings, it is important to gain more insights into the driving forces for the formation of different crystal phases and variations in layer stacking in InGaAs NWs. Generally, WZ and ZB polytypes have only very small energy differences in both binary constituents, i.e., ~12 meV/atom (for GaAs) and ~5 meV/atom (for InAs), and further comprise atomically identical (0001) and {111} facets [83]. Therefore, the stabilization of WZ phase in III–V semiconductor NW is quite readily achieved as the {110} side facets contribute to overall lower surface free energies, which particularly occurs for small NW diameters [83]. However, the above mentioned reports on InGaAs NW point clearly to discrepancies in the diameter-dependent stabilization criteria of the dominant crystal structure. This suggests that besides the thermodynamic stability criteria also kinetic effects (V/III ratio, temperature, surfactants, etc.) and the predominant growth mechanism must play a very critical role in the relative stability of the WZ phase in our present NWs. Recently, we performed growth temperature-dependent investigations of the crystal phase and found that for a fixed InGaAs composition higher temperature leads to a more pronounced WZ stacking with longer segments as opposed to growth at lower temperature [76]. This suggests that the trends in crystal phase stacking observed here are much more likely dominated by growth temperature than by the composition. Further tuning of both growth temperature and V/III ratio for each individual InGaAs composition is

Phys. Status Solidi RRL **8**, No. 1 (2014)

21

therefore required to optimize the crystal structure towards higher phase purity. While systematic studies do not yet exist for catalyst-free, VS-type In(Ga)As NWs, extensive investigations of the growth parameter space and the effect on crystal phase modifications have been performed for VLS-grown In(Ga)As NWs [84]. However, in the latter case the dynamics for crystallization of different phases and changes in stacking sequence are largely dominated by super-saturation effects (V/III ratio) of the catalyst particle, and thus might be difficult to compare with non-catalytically grown NWs.

4 Optical properties of InGaAs nanowires To date, only very little information exists about the electronic and optical properties of InGaAs NWs. This is primarily due to the fact that in most studies it has been very difficult to achieve the compositional uniformity necessary to clearly differentiate between electronic effects arising from chemical features (i.e., fluctuations in alloy composition) with those due to microstructural characteristics (i.e., different crystal phases, defects) in ternary InGaAs NWs. This has limited access to fundamental intrinsic structure property correlations in InGaAs NWs. Consequently, for binary GaAs and InAs NWs it is much more straightforward to correlate structural modifications (e.g. WZ vs. ZB phases) and different stacking configurations (phase mixing, polytypism, stacking faults, etc.) with the electronic bandstructure and further provide links to the optical emission properties [85–87]. In this respect, several studies were conducted to elucidate the band gap energy difference between the WZ and ZB phase of GaAs NWs [86, 88–91]. Nevertheless, even for the binary system the obtained results are still highly controversial: Whereas most reports suggest that the band gap energy of WZ-GaAs is ~30–55 meV larger than the one of bulk ZB GaAs [86, 88–90], others state that the WZ-GaAs band gap is slightly smaller or similar to the ZB band gap [91, 92]. For InAs NWs, very limited information has been gained so far, because of well-known difficulties of PL spectroscopy in the IR spectral range. While the theoretically estimated band gap energy of WZ-InAs is approximately ~40–55 meV higher than the respective ZB-InAs value [88, 89], recent reports on phase-pure WZ InAs NWs were contradicting, i.e., stating that the respective band gap energy is either similar to the ZB phase [93] or substantially larger (>100 meV) [94].

In the following, systematic investigations of the structure-dependent band gap properties of composition-tuned site-selective InGaAs NW arrays are performed for the first time. The major advantage in using highly periodic, site-selective InGaAs NW arrays is that these show negligible size and composition fluctuations, allowing extraction of fundamental information about the electronic structure from ensemble measurements such as in PL spectroscopy. For such measurements we used a home-built PL setup specifically designed for the IR spectral region, using a He/Ne laser (633 nm) for excitation along with a mono-

chromator and a liquid nitrogen cooled InSb photodetector on the analysis side. Further experimental details can be found elsewhere [76]. The excitation laser spot size focused onto the sample had a spot diameter of ~2 μm, corresponding to an excitation volume of ~50–60 NWs. It is important to note, that due to the high-periodicity growth the NW density and hence excitation volume was similar for all investigated samples (within a factor of ~2 considering small changes in NW volume), allowing direct comparison of emission intensities among different samples.

Characteristic PL spectra of all investigated InGaAs NW samples normalized to the intensity of the binary InAs NW reference sample are shown in Fig. 7(a) as recorded at low temperature (4 K) and identical excitation power. As expected, the PL spectra shift to higher emission energies with increasing Ga content x(Ga), with their peak energies and integrated PL intensity plotted in Fig. 7(b). Interestingly, the PL linewidths are similar among the In-rich InGaAs NW samples with x(Ga) = 0, 0.07 and 0.19, however, much broader linewidths (factor of ~2) are observed for the sample with x(Ga) = 0.36. The lower end of our measured linewidths are well comparable to the state-of-the-art of the narrowest reported low-T linewidths obtained for single [3] or few InGaAs NWs (<15 NWs) [67], despite the much higher NW density measured here. The independence of the linewidths from the Ga-content in the first three samples indicates that the compositional features are not responsible for the peak broadening. This is expected considering the very uniform compositional homogeneity and negligible phase separation in these NWs, as confirmed by XRD and EDXS. Instead, the linewidth is most likely limited by defect states, impurities as well as possible surface states, considering that these NWs have a large stacking defect density and are not passivated. In particular, the increased linewidth for the sample with x(Ga) = 0.36 suggests that the stacking defects play a dominant role, since this sample shows a significantly larger stacking disorder as opposed to the other three samples (compare Fig. 6).

The measured PL peak energy of all respective InGaAs NW samples is further compared with the expected composition-tunable band gap energy dependence of bulk (ZB) InGaAs (Fig. 7b). Most interestingly, the PL peak energies of all three In-rich InGaAs NW samples are blue shifted by ~30–45 meV with respect to the bulk energy values, whereas the NW sample with the highest Ga-content (x(Ga) = 0.36)) matches with the bulk value [76]. Several reasons can be considered to produce such characteristic blue-shift in the In-rich InGaAs NWs: (a) strong band-filling effects, (b) radial quantum confinement, and (c) band gap differences due to the underlying WZ crystal phase.

As recently reported, band filling effects were found to be very small in these NWs producing blue-shifts of typically less than 10 meV, even for very high laser excitation power densities [76]. In addition, radial size quantization
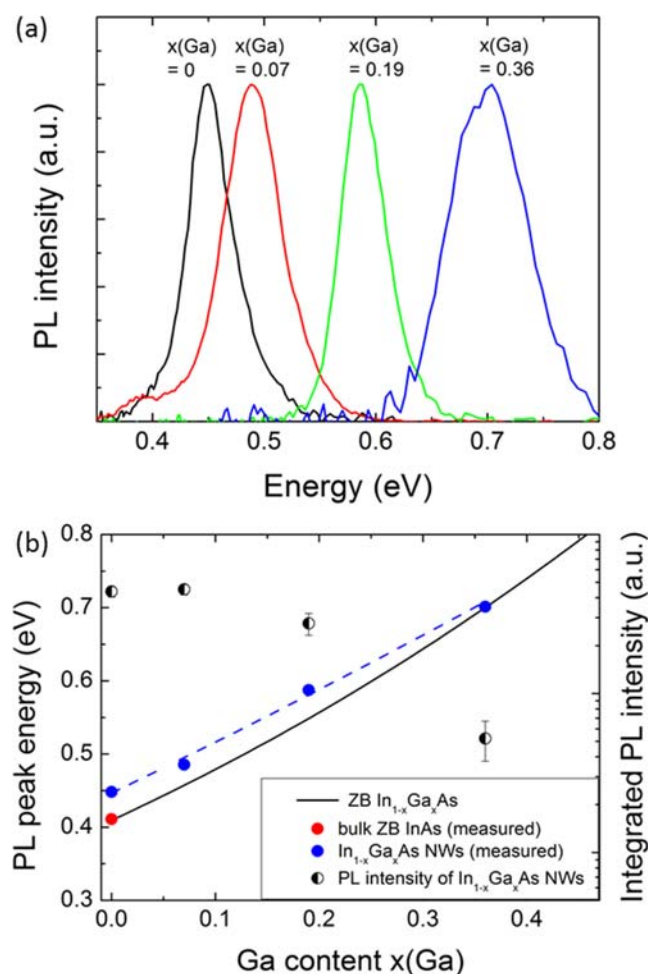
Figure 7 (a) Normalized PL spectra of site-selectively grown composition-tuned InGaAs NW arrays on NIL-SiO$_2$/Si(111), as measured at low-temperature (4 K) and excitation power of 690 μW. The Ga-content x(Ga) associated with the different spectra was determined by XRD. (b) Corresponding PL peak energies (blue symbols) and integrated PL intensity (half-open symbols) for these InGaAs NW arrays as a function of Ga-content x(Ga). For comparison also the expected band-gap energy dependence of bulk ZB InGaAs (Ref. [97]) is shown (solid black line). In addition, the peak energy position of a bulk ZB InAs reference (x(Ga) = 0) as measured under identical conditions is plotted (red symbol), verifying the used formalism for the composition-dependence of the band gap in bulk InGaAs. Most strikingly, for the In-rich InGaAs NWs the peak energies are ∼30–45 meV higher than the respective bulk value which is ascribed to the underlying WZ-based crystal phase. Reprinted with permission from Ref. [76], Copyright (2013) by American Physical Society.

effects can also be ruled out since they only become relevant in In-rich In(Ga)As NWs for NW diameters below ∼60 nm [95], much smaller than the structures investigated here. Therefore, the observed blue-shift can be most likely ascribed to the theoretically predicted higher band gap energy of WZ-phase InGaAs [88, 89, 96], which has been

clearly identified in the corresponding TEM data of Fig. 6 for the three In-rich InGaAs NWs. The absence of the blue-shift in the sample with the highest Ga content x(Ga) = 0.36 correlates also well with the structural data, namely that no WZ phase could be identified in this case and the microstructure was governed by heavy stacking disorder. This sensitivity of the optical emission on the microstructural properties is also reflected in the integrated PL peak intensity (Fig. 7b). High emission intensities were found for the three In-rich InGaAs NW samples, whereas the higher-Ga content NW sample yielded ∼10× weaker emission intensity due to the much higher defect density [76].

A remaining question that immediately arises is whether the measured blue-shift in the In-rich InGaAs NWs is directly representing the true low-temperature WZ band gap of InGaAs. To resolve this question, Fig. 8 compares the temperature-dependent PL spectra (a) and peak energy (b) of a WZ-phase InGaAs NW array (x(Ga) = 0.19) with the expected band gap shrinkage (Varshni behavior) for bulk ZB InGaAs assuming identical composition [97]. Whereas the classical Varshni behavior for bulk InGaAs indicates the expected continuous decrease in band gap energy with temperature [97], the PL peak energies of the InGaAs NWs evidence saturation and hence a delayed Varshni dependence at low temperature. This anomalous behavior was also found for all other investigated NW samples, and was attributed to the presence of localized trap states near the band edge primarily due to the high number of stacking defects [76]. These localized states get excited upon increasing temperature, whereby the photocarriers get lifted from the low energy trap states to the band edge, a process that is in competition with the lowering of the band gap (Varshni behavior) at increased temperature. Therefore, the PL peak energies as measured at low temperature likely underestimate the precise position of the band edge. As a consequence, the true band gap energies of the WZ phase InGaAs NWs might be even higher than given by the measured ∼30–45 meV blue-shift.

Murayama et al. [88] and Zanolli et al. [89] calculated that the low-temperature band gap energy of WZ phase InAs is about ∼40–55 meV higher than the band gap value of bulk ZB InAs. Recent investigations of mixed-phase (WZ-ZB) InAs NWs estimated a low-T band gap energy of ∼0.46 eV for WZ-InAs, utilizing interpolation methods from excitation power-dependent data across the type-II crystal-phase boundaries between mixed WZ-ZB InAs phases [100]. On the other end, the theoretically predicted band gap of WZ-GaAs is considered ∼20–35 meV higher in energy than the respective ZB counterpart [88, 89, 96]. Therefore, for composition-tuned WZ-phase InGaAs the expected band gap energy difference from the bulk ZB reference should be somewhere within the range of ∼20–55 meV, depending on composition. This is in good agreement with the range of blue-shifts as observed experimentally in our study on WZ-InGaAs NW arrays.

Phys. Status Solidi RRL **8**, No. 1 (2014)

Review
@ RRL

23
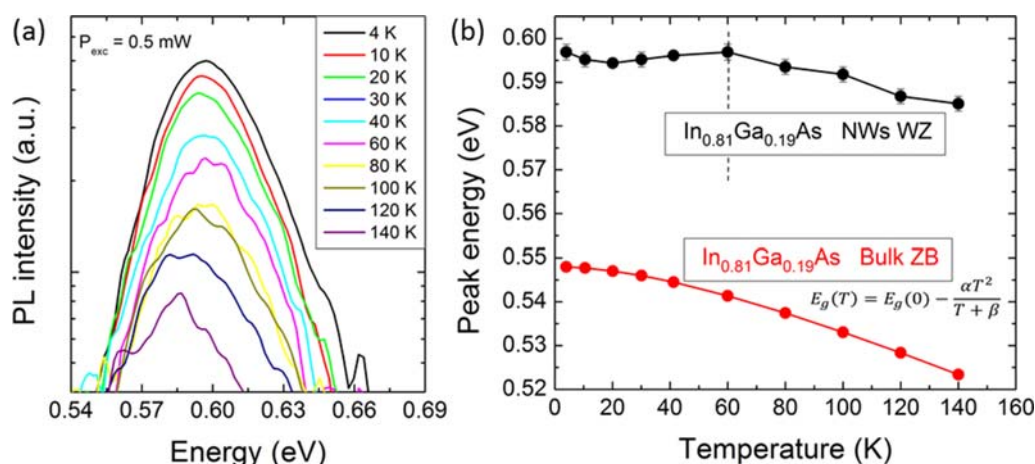
Figure 8 (a) Temperature (*T*)-dependent PL spectra shown for the InGaAs NW sample with *x*(Ga) = 0.19 (measured at excitation power of 690 μW). (b) Corresponding *T*-dependent shift in PL peak energy of the InGaAs NWs in comparison with the classical Varshni-like band gap shrinkage of bulk ZB InGaAs. The Varshni formalism is described by the function in the inset (see also Refs. [98, 99]). The evolution of the PL peak energy of the InGaAs NWs shows a characteristic delay in the band gap shrinkage up to ∼60 K due to the presence of stacking-fault related localized trap states. Reprinted with permission from Ref. [76], Copyright (2013) by American Physical Society.

5 InGaAs/Si heterojunction diode characteristics The vertical integration of III–V-based NWs on Si substrate is a promising strategy to circumvent the various limitations faced by heteroepitaxial growth of planar III–V's on Si over the last few decades. Large lattice and thermal mismatches as well as the polar versus non-polar nature of the (In,Al,Ga)As–Si heteroepitaxial system are known to cause misfit and threading dislocations, antiphase domains and boundaries in planar structures. However, in the NW geometry the strain relaxation constraints are significantly alleviated particularly when the NW diameters become small. Various reports based on critical dimension considerations for strained growth of NWs on foreign substrates or in axial NW heterostructures demonstrate that dislocation-free growth of III–V NWs is feasible even in systems of very large lattice mismatch [11, 101–103].

This advantage has enabled not only dislocation-free growth of III–V NWs on Si, but more importantly, offers the flexibility to build highly integrated III–V-based devices on Si platform, such as e.g. light emitting diodes (LEDs) [104, 105] and nanolasers [106], high-performance wrap-gate field effect transistors (FETs) [5, 107, 108], or even photovoltaic devices employing the III–V NW/Si heterojunction [109]. In such III–V NW-on-Si devices particularly the use of ternary InGaAs NWs is very attractive because of the intrinsically high electron mobility and tunable band gap of InGaAs as well as the adaptive nature to versatile heteroepitaxial systems (e.g., InGaAs/GaAs and InGaAs/InP) and the relatively easy formation of low-resistance Ohmic contacts. Recently, this has been impressively demonstrated e.g. in enhanced on/off-current performance of free-standing wrap-gate InGaAs channel NW-FETs on Si employing radial multishell InGaAs–InP/InAlAs heterostructures [5]. Devices utilizing the

charge carrier transport across the InGaAs-NW/Si hetero-interface provide additional means to explore new device functionalities. For instance, vertically integrated n-type InAs NW heterojunctions on p-type Si substrate have shown good state-of-the-art rectification ratio ($> 10^4$ at ±0.5 V), ideality factors of 1.5 and low p–n diode leakage currents ($\sim 10^{-8}$ A), offering large potential for broadband vertical array-like photovoltaic and photodetection devices [109, 110]. Furthermore, p–n heterojunctions based on p-type GaAs NWs on n-type Si substrate showed also relatively good ideality factors (<2) and enabled the fabrication of high-speed avalanche photodiodes (APD) with very large multiplication factors [111]. These optoelectronic device results are a first indication that the (In,Ga)As-NW/Si substrate system allows decent quality heterointerfaces.

Another major device building upon heavily doped (In,Ga)As NW/Si p–n heterojunctions is the tunneling FET, which is expected to leverage very power-efficient transistors operating at low supply voltages (sub-0.5 V), fast switching speeds and reduced subthreshold swing (SS < 60 mV/dec) [112, 113]. Here, the integration of narrow-gap NW materials (InAs, InGaAs, . . .) with very high interband tunneling on Si substrate is particularly desired, in order to exploit the mature and cost-efficient Si-based CMOS device fabrication technology and further allow ultra-high density integration [114, 115]. First reports based on heavily doped p-Si/n-InAs NW tunnel junctions indicated already very high tunnel currents, demonstrating their suitability as key components for future NW-based TFETs [114–116].

Obviously, one of the major ingredients of such devices is the p–n junction or tunnel junction, i.e., the respective (In,Ga)As NW/Si heterojunction itself. Therefore in the following a detailed investigation of the current (*I*)–voltage (*V*) characteristics (at room-temperature) of in-

dividual In(Ga)As–NW/Si heterojunction diodes is presented to gain further insights into the various features of these heterointerfaces. First, we present results as obtained from self-assembled n-type InAs and InGaAs NWs on SiO_x-masked p-type Si(111) substrate and further discuss the challenges for site-selectively grown NW/Si heterojunctions.

In order to determine the I–V characteristics of the self-assembled NWs, we needed to establish a methodology allowing contacting and probing of individual NWs in their directly integrated free-standing geometry on Si. Due to the high density and small interwire distance (200–500 nm) of self-assembled NWs it is technologically very challenging to fabricate individual contacts to single NWs. Instead, we utilized the unique method of conductive atomic force microscopy (cAFM) which employs a positionable nm-sized tip (local electrode) to the sample surface and thus probes the local electrical properties with a spatial resolution in the range of a few tens of nanometers [117]. A schematic illustration of the applied measurement principle of cAFM is shown in Fig. 9(a), while further experimental details are listed in Ref. [4]. It is important to note that since the cAFM operates in constant contact mode, the free-standing NWs can easily get removed from the substrate surface by the exerted forces during scanning. Hence, the NWs were embedded in an insulating benzocyclobutene (BCB) layer, which was etched back to a certain thickness so that the NWs protrude by $\sim$50–90 nm from the BCB layer [4]. The second contact on the backside of the p-type Si substrate was formed by silver (Ag) paste to establish two-terminal I–V profiling of the n-In(Ga)As-NW/p-Si heterojunction diodes. Here, the current is measured by the local conductive tip after a certain bias voltage was applied to the back contact. All measurements were performed in dark and under otherwise identical conditions (scan rate $\sim$0.5–1 Hz, constant contact force of 180 nN).

Since the measurements were conducted in scanning constant contact mode, both topography and current maps could be profiled simultaneously, exemplified in Fig. 9(b), (c) for InAs NWs on heavily doped p^{++}-Si substrate ([p] $\sim 7 \times 10^{19}$ cm^{-3}). The bright, high-contrast spots represent the individual NWs, showing very good spatial correlation between the two images and further reflect the typical NW densities obtained for such self-assembled growth processes on SiO_x-masked Si(111) templates. To probe the I–V characteristics of individual NWs more closely, the cAFM tip can be adjusted to fixed positions while voltage sweeps from reverse to forward bias and vice versa are performed.

In the first set of experiments the I–V diode characteristics of individual intrinsically n-type InAs NW/p-type Si diodes were evaluated as a function of the p-type substrate doping level (range of $\sim 10^{16}$ to high-10^{19} cm^{-3}). In this set the InAs NWs had all similar lengths ($\sim$0.7–0.9 µm) and diameters ($\sim$40–65 nm), and the intrinsic n-type doping level was assumed in the 10^{17} cm^{-3} range based on previ-
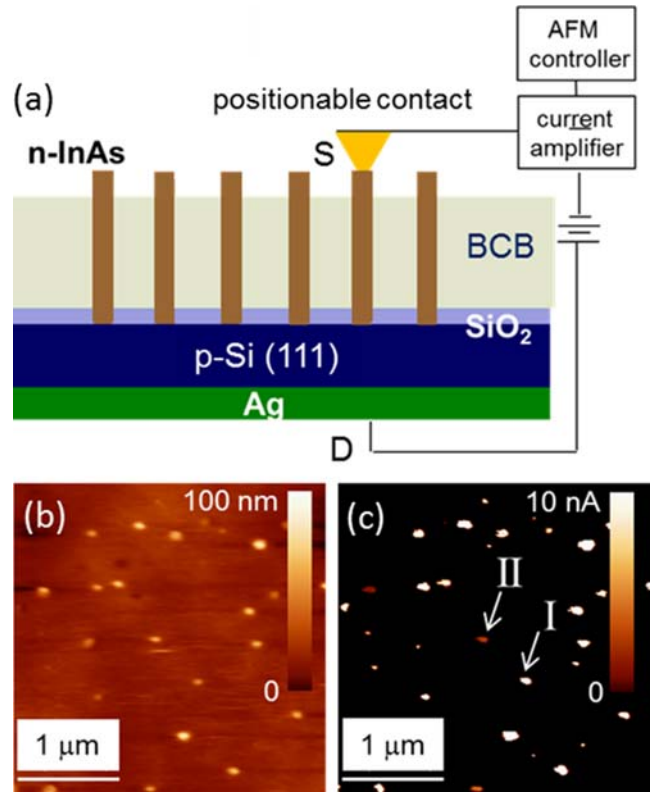
Figure 9 (a) Schematic illustration of the measurement geometry of cAFM for freestanding n-(In,Ga)As NW/p-Si diodes. The contacts for the two-terminal I–V profiling are realized by an Ag back electrode to the p-Si substrate and a nm-sized positionable electrode (Pt/Ir-tip) to the n-In(Ga)As NWs. To guarantee damage-free scans the NWs are embedded almost along their entire length into a supporting BCB layer. (b) Topography and (c) respective current map (recorded under $V_{SD} = 200$ mV forward bias) of a representative self-assembled NW sample, consisting of InAs NWs grown on heavily doped p^{++}-Si ($\sim 7 \times 10^{19}$ cm^{-3}). The current map shows a large number of high-contrast current spots (type-I diode) and smaller number of weak-contrast current spots (type-II diode) marked by arrows. Reprinted with permission from Ref. [4], Copyright (2012) by American Physical Society.

ous FET measurements [4]. Figure 10(a) shows representative I–V curves, providing insights into the various features of the individual p–n diodes for different substrate doping levels. For very low p-type doping of the Si substrate ([p] $\sim 1 \times 10^{16}$ cm^{-3}) (black curve) we observe strongly asymmetric transfer curves, evidencing classical p–n diode behavior with ideality factors of $\eta \sim 2$–4 and a rectification ratio of $\sim 10^2$ at ±0.5 V. Raising the doping level to $\sim 9 \times 10^{18}$ cm^{-3} (red curve) gives larger forward current, but only a marginal increase in reverse current at low reverse bias (-0.5 V $< V_{SD}$). Ultimately, for the highest doping level of $\sim 7 \times 10^{19}$ cm^{-3} (uppermost blue curve, i.e., type-I diode) strong interband tunneling is observed consistent with the highly symmetric transfer characteristics. At reverse bias conditions, the current is thus increased by $\sim$4 orders of magnitude with respect to the classical p–n diode

Phys. Status Solidi RRL **8**, No. 1 (2014)

Review
@ RRL

25
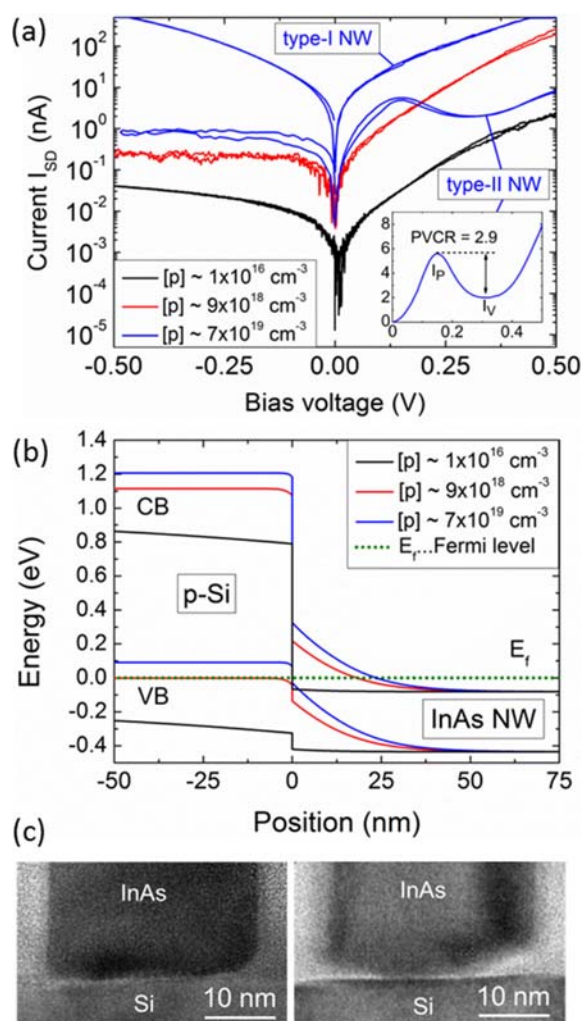
Figure 10 (a) *I–V* curves of representative self-assembled n-InAs NW/p-Si diodes as a function of the p-type substrate doping level ([p] $\sim 1 \times 10^{16}$ cm^{-3} – $\sim 7 \times 10^{19}$ cm^{-3}). For very high p-type doping ($\sim 7 \times 10^{19}$ cm^{-3}) two types of *I–V* curves can be distinguished, related to type-I and type-II tunnel diodes as also seen in Fig. 9(c). The inset further shows the characteristic negative differential resistance (NDR) of this type-II tunnel diode (PVCR $\sim$2.9) which represents an Esaki tunnel diode. (b) Band profile simulations of the n-InAs/p-Si heterojunction for three different p-type doping levels using "nextnano3". The Fermi level position relative to the CB and VB of InAs and Si, respectively, is indicated as dashed line. (c) Cross-sectional TEM micrographs of freestanding InAs-NW-on-Si showing two types of heterointerfaces with different widths and likely different misfit dislocation densities. Reprinted with permission from Ref. [4], Copyright (2012) by American Physical Society.

current, yielding $\sim$600 nA at –0.5 V that corresponds to a current density of $\sim$45 kA/cm^2 (assuming that the current runs uniformly through the cross-section of the NW). This is in very good agreement with data reported previously for nominally undoped InAs NWs on heavily doped p-type Si as grown by MOCVD [114]. To explain these tunnel-junction diode characteristics, band profile simulations

were performed for the p-Si/n-InAs heterojunction in dependence on p-type substrate doping level (see Fig. 10b) [4]. The simulations confirm that for heavy substrate doping the Fermi level shifts to below the valence band (VB) of the p-Si (while the Fermi level is fixed above the conduction band (CB) on the n-InAs side), such that electrons from the VB in the p-side tunnel readily to the CB in the n-side at low reverse bias.

Interestingly, besides this characteristic "type-I" tunnel diode we also observed a small number of tunnel diodes (referred to as "type-II" diodes) with a characteristic negative differential resistance (NDR) in the forward bias direction (see Fig. 10a, blue curve and inset), which is strong evidence for Esaki tunneling. The existence of both types of diodes was only observed in the tunneling regime, i.e., for the highest p-type substrate doping level. The particular Esaki diode shown in Fig. 10a has a record high peak-to-valley-current ratio (PVCR) of 2.92 for the InAs/Si system at room temperature, demonstrating that the p–n junction is very abrupt and of high quality. To explain the coexistence of tunnel diodes with and without NDR in the same sample, recent observations attributed this to differences in misfit defect concentrations at the n-InAs/p-Si heterointerface [114, 118]. Figure 10(c) represents two typical cross-sectional TEM micrographs across the p-Si/n-InAs heterointerface, showing that the basal width of the NW differs from NW to NW, most likely as a result of the statistical nature of pinhole formation in the SiO$_x$ mask layer and the subsequent self-assembled growth process. The different basal widths (i.e., p–n junction neck area) would thus represent different misfit dislocation densities at these heterointerfaces and may result in the two characteristic types of tunnel diodes. Particularly, the image shown on the right-hand side evidences a neck region of <10 nm, suggesting that there might be no or only very few misfit dislocations such that good Esaki-type tunnel diodes can be formed. On the other hand, the absence of NDR is likely due to high excess currents governed by a high density of defect states within the band gap [118, 119].

Obviously, it is thus much desired to reduce the basal width of the NW nucleation zone as much as possible, which might be achieved by drastically down-scaling the NW diameter. Therefore, in another set of experiments we varied the NW diameter from 90 nm down to 25 nm by tuning the growth conditions and using again heavily p-type doped Si(111) ([p] $\sim 7 \times 10^{19}$ cm^{-3}) as substrates. Figure 11 shows the typical Esaki-type p–n diode characteristics for self-assembled NW samples with three different average NW diameters of 90 nm, 45 nm and 25 nm (also shown in the respective SEM images).

As expected, reducing the NW diameter from 90 nm to 45 nm results in a distinct increase in PVCR from $\sim$1.0–1.4 to maximum values of $\sim$2.9, while also the peak current density (PCD) increases to $\sim$0.5 kA/cm^2. However, further reduction of the NW diameter to *d* $\sim$25 nm does not yield further improvement in PVCR and PCD. This implies that not necessarily the NW diameter itself governs the NDR
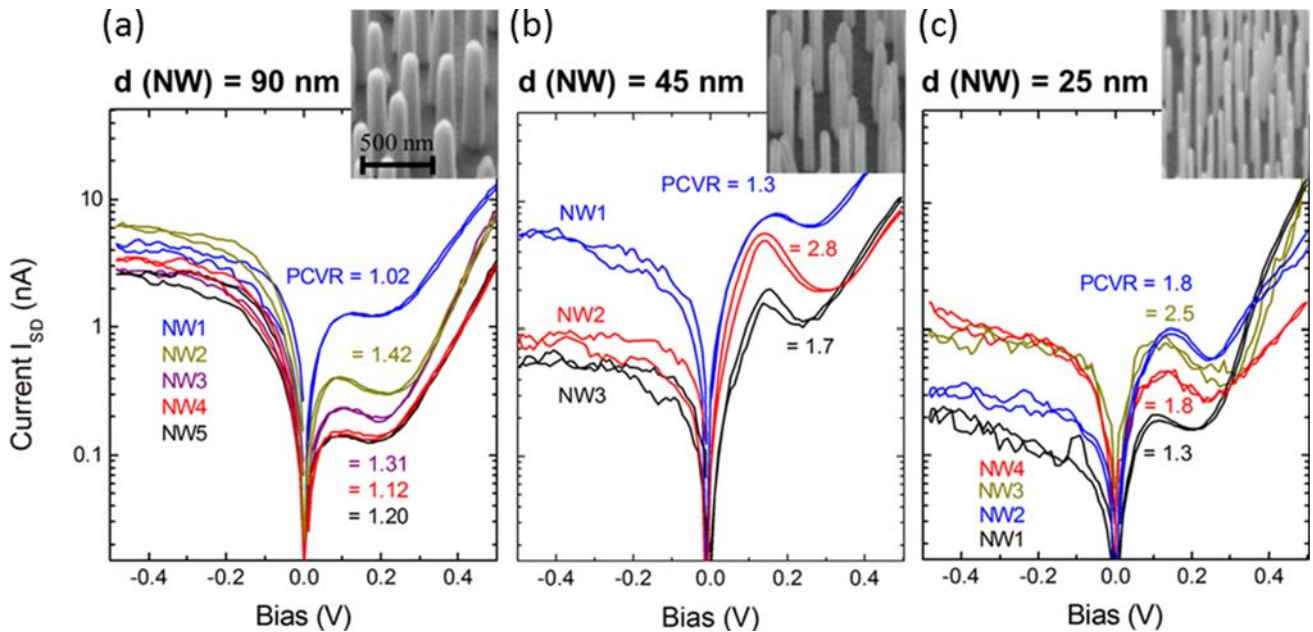
Figure 11 Esaki tunneling diode characteristics of n-InAs NWs on heavily p-type doped Si ($[p] \sim 7 \times 10^{19}$ cm^{-3}) for three different average NW diameters (a) $d \sim 90$ nm, (b) $d \sim 45$ nm, and (c) $d \sim 25$ nm. The insets in the upper right corners of each figure illustrate SEM images of the as-grown NWs. Reprinted with permission from Ref. [4], Copyright (2012) by American Physical Society.

characteristics, but the basal width at the the InAs-NW/Si interface and corresponding number of associated defects might be the limiting factor. This is supported by the fact that even in the sample with the thinnest NWs both type-I and type-II tunnel diodes occurred due to the statistical nature of the SiO$_x$ pinhole formation, leading to high interfacial defect concentrations and high excess currents that obscure the observation of NDR. In order to achieve consistently Esaki-type diodes with much higher PVCR and PCD, we believe that the NW diameters and p–n neck regions need to be controlled to below 10 nm.

Recently, we also suggested that instead of downscaling the NW diameters, another strategy to reduce misfit defect concentrations at the NW/Si interface is to modify the lattice mismatch by using ternary InGaAs NWs (i.e., $\Delta a/a^{(\text{GaAs/Si})} \sim 4\% < \Delta a/a^{(\text{InGaAs})} < \Delta a/a^{(\text{InAs/Si})} \sim 11.6\%$) [4]. Such efforts are expected to allow for NDR with good PVCR at comparatively larger NW diameter. Indeed, NDR with very good PVCR was observed when increasing Ga content, yielding e.g. PVCR as high as 2.6 for x(Ga) = 0.16 at moderate NW diameters of $\sim$60 nm (see Fig. 12). However, increasing the Ga content too far also reduces the tunneling current due to an increase in band gap, such that the ideal heterojunction tunnel diode will require optimization of both lattice mismatch as well as p–n junction neck region as well as controlled doping of the NW.

As discussed before, avoiding the large fluctuations in tunnel diode characteristics (type-I versus type-II NW diodes) as obtained from self-assembled growth processes would be important for future and better control of Esaki tunnel diode performance. Obviously, site-controlled

growth of periodic InGaAs NW arrays from well-defined mask openings is therefore a very promising strategy. Recently, we have conducted first experiments using high-periodicity n-type InAs NW arrays on heavily p-type doped Si(111) substrates using a $\sim$20 nm thin SiO$_2$ mask with hole patterns of 80 nm diameter. Surprisingly, the resulting tunnel current densities were $\sim$10^1–10^2 times lower than those obtained from self-assembled growths, and no NDR could be observed so far. There are two reasons which may explain the currently relatively poor-quality heterointerfaces in site-selectively produced NW samples. First, the diameters of the SiO$_2$ mask openings were $\sim$80 nm, i.e., much wider than the nm-sized pinholes in the self-assembled process. This is expected to lead to much wider basal widths of the In(Ga)As-NW/Si heterojunction and hence higher interface defect concentrations.

Secondly, to fabricate the mask openings reactive ion etching (RIE) was employed, although the etching was not performed entirely down to the Si substrate surface. Instead the RIE etching process was terminated a few nm above the Si interface, while the remaining SiO$_2$ was removed wet chemically using buffered HF solution to keep the substrate interface intact [70]. Nevertheless, the employed ions may have caused an energy transfer into the Si substrate, thus deteriorating the p–n junction by e.g. introducing further defects. Further experiments are therefore needed to circumvent the RIE etching process while effectively reducing the mask opening diameter to sizes of well below 20 nm.
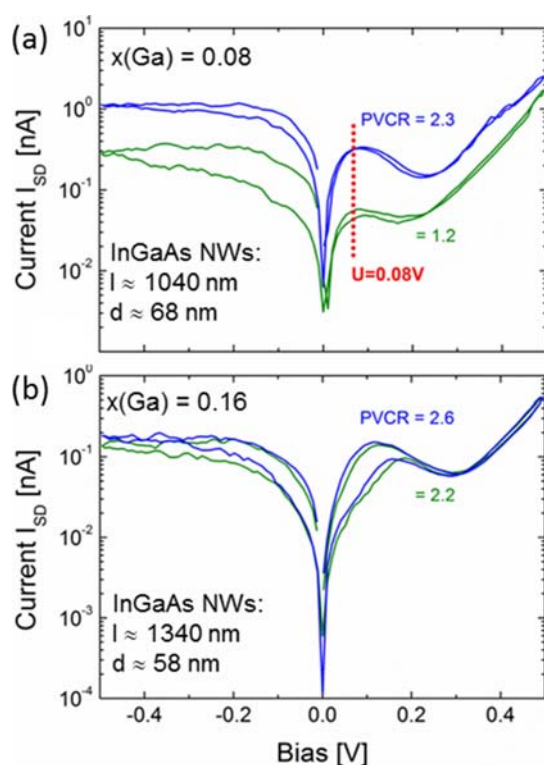
Figure 12 *I–V* curves of n-InGaAs NW/p^{++}-Si Esaki tunnel diodes for two different Ga contents of (a) *x*(Ga) = 0.08 and (b) *x*(Ga) = 0.16. Note that for increased Ga content the NDR is well preserved reaching PVCR as high as 2.6 for an InGaAs composition of *x*(Ga) = 0.16. Reprinted with permission from Ref. [4], Copyright (2012) by American Physical Society.

6 Summary In this review, we summarized recent progress in the growth of free-standing ternary InGaAs NWs with an emphasis on vertical integration on a Si platform. Starting with conventional catalyst-assisted growth (Au- or self-catalyzed), we showed that the underlying vapor–liquid–solid (VLS) growth process leads to significant morphological and compositional instabilities complicating the formation of homogeneous InGaAs NWs. In contrast, catalyst-free vapor–solid (VS) growth processes eliminate several of these issues, allowing the spontaneous formation of non-tapered, composition-tuned InGaAs NW arrays with uniform compositional distribution across the entire NW lengths. A comparison between spontaneous, self-assembled growth of randomly positioned InGaAs NWs and selective area growth (SAG) of high-periodicity InGaAs NWs on pre-patterned Si(111) substrates further evidences extremely high compositional uniformity not only across single NWs but also over the entire NW array for the SAG process.

These findings enabled fundamental structure-property correlation measurements and thus extraction of several important electronic properties, such as crystal phase dependent band gap energy, from ensemble photoluminescence (PL) spectroscopy. The data presented here confirms unambiguously that the underlying wurtzite (WZ) crystal phase of the InGaAs NWs results in a wider band gap energy, which is at least ~30–45 meV larger than the respective zincblende (ZB) counterpart, thus clarifying several discrepancies reported previously. Moreover, this review also addressed quality issues of the InGaAs/Si heterointerface and highlighted that due to the small NW footprint interface defect concentrations can be minimized. This is particularly emphasized in measurements of the p–n diode characteristics of single heavily doped p-Si/n-InGaAs-NW heterojunctions that enable distinct Esaki-type tunneling behavior and negative differential resistance with record high room-temperature peak-to-valley current ratios of ~3. These recent improvements in growth and compositional uniformity control as well as the feasibility of high-quality InGaAs/Si heterointerfaces demonstrated in this review are expected to drive forward several integrated III–V-on-Si device technology concepts.

References

[1] J. C. Shin, K. H. Kim, K. J. Yu, H. Hu, L. Yin, C.-Z. Ning, J. A. Rogers, J.-M. Zuo, and X. Li, Nano Lett. **11**, 4831 (2011).

[2] R. Chen, T.-T. D. Tran, K. W. Ng, W. S. Ko, L. C. Chuang, F. G. Sedgwick, and C. Chang-Hasnain, Nature Photon. **5**, 170 (2011).

[3] M. Moewe, L. C. Chuang, S. Crankshaw, K. W. Ng, and C. Chang-Hasnain, Opt. Express **17**, 7831 (2009).

[4] T. Yang, S. Hertenberger, S. Morkötter, G. Abstreiter, and G. Koblmüller, Appl. Phys. Lett. **101**, 233102 (2012).

[5] K. Tomioka, M. Yoshimura, and T. Fukui, Nature **488**, 189 (2012).

[6] J. Tatebayashi, Y. Ota, S. Ishida, M. Nishioka, S. Iwamoto, and Y. Arakawa, Appl. Phys. Lett. **100**, 263101 (2012).

[7] A. C. Scofield, S.-H. Kim, J. N. Shapiro, A. Lin, B. Liang, A. Scherer, and D. L. Huffaker, Nano Lett. **11**, 5387 (2011).

[8] K. Hiruma, H. Murakoshi, M. Yazawa, and T. Katsuyama, J. Cryst. Growth **163**, 226 (1996).

[9] X. Duan and C. M. Lieber, Adv. Mater. **12**, 298 (2000).

[10] M. S. Gudiksen, L. J. Lauhon, J. Wang, D. C. Smith, and C. M. Lieber, Nature **415**, 626 (2002).

[11] T. Mårtensson, C. P. T. Svensson, B. A. Wacaser, M. W. Larsson, W. Seifert, K. Deppert, A. Gustafsson, L. R. Wallenberg, and L. Samuelson, Nano Lett. **4**, 1987 (2004).

[12] E. P. A. M. Bakkers, J. A. Van Dam, S. De Franceschi, L. P. Kouwenhoven, M. Kaiser, M. Verheijen, H. Wondergem, and P. Van der Sluis, Nature Mater. **3**, 769 (2004).

[13] R. S. Wagner and W. C. Ellis, Appl. Phys. Lett. **4**, 89 (1964).

[14] K. A. Dick, K. Deppert, L. Samuelson, and W. Seifert, J. Cryst. Growth **297**, 326 (2006).

[15] L. C. Chuang, M. Moewe, C. Chase, N. P. Kobayashi, C. Chang-Hasnain, and S. Crankshaw, Appl. Phys. Lett. **90**, 043115 (2007).

[16] M. Tchernycheva, L. Travers, G. Patriarche, F. Glas, J. C. Harmand, G. E. Cirlin, and V. G Dubrovskii, J. Appl. Phys. **102**, 094313 (2007).

[17] S. A. Dayeh, E. T. Yu, and D. Wang, Nano Lett. **7**, 2486 (2007).

[18] Z. H. Wu, X. Y. Mei, D. Kim, M. Blumin, and H. E. Ruda, Appl. Phys. Lett. **81**, 5177 (2002).

[19] N. Skold, L. S. Karlsson, M. W. Larsson, M. E. Pistol, W. Seifert, J. Tragardh, and L. Samuelson, Nano Lett. **5**, 1943 (2005).

[20] P. Paiano, P. Prete, N. Lovergine, and A. M. Mancini, J. Appl. Phys. **100**, 094305 (2006).

[21] S. G. Ihn, J. I. Song, T. W. Kim, D. S. Leem, T. Lee, S. G. Lee, E. K. Koh, and K. Song, Nano Lett. **7**, 39 (2007).

[22] Y. Kim, H. J. Joyce, Q. Gao, H. H. Tan, C. Jagadish, M. Paladugu, J. Zou, and A. Suvorova, Nano Lett. **6**, 599 (2006).

[23] I. Regolin, V. Khorenko, W. Prost, F. J. Tegude, D. Sudfeld, J. Kästner, and G. Dumpich, J. Appl. Phys. **100**, 074321 (2006).

[24] H. J. Joyce, Q. Gao, J. Wong-Leung, Y. Kim, H. H. Tan, and C. Jagadish, IEEE J. Select. Top. Quantum Electron. **17**, 766 (2011).

[25] H. Ye, Z. Y. Yu, S. Kodambaka, and V. B. Shenoy, Appl. Phys. Lett. **100**, 263103 (2012).

[26] D. M. Cornet and R. R. LaPierre, Nanotechnology **18**, 385301 (2007).

[27] M. Paladugu, J. Zou, Y. Guo, X. Zhang, Y. Kim, H. J. Joyce, Q. Gao, H. H. Tan, and C. Jagadish, Appl. Phys. Lett. **93**, 101911 (2008).

[28] J. Bauer, V. Gottschalch, H. Paetzelt, and G. Wagner, J. Cryst. Growth **310**, 5106 (2008).

[29] F. Jabeen, V. Grillo, F. Martelli, and S. Rubini, IEEE J. Sel. Top. Quantum Electron. **17**, 794 (2011).

[30] Y. N. Guo, H. Y. Xu, G. J. Auchterlonie, T. Burgess, H. J. Joyce, Q. Gao, H. H. Tan, C. Jagadish, H. B. Shu, X. S. Chen, W. Lu, Y. Kim, and J. Zou, Nano Lett. **13**, 643 (2013).

[31] M. Palagudu, J. Zou, X. Zhang, Y. Kim, H. J. Joyce, Q. Gao, H. H. Tan, and C. Jagadish, Appl. Phys. Lett. **93**, 101911 (2008).

[32] J. C. Shin, D. Y. Kim, A. Lee, H. J. Kim, J. H. Kim, W. J. Choi, H. S. Kim, and K. J. Choi, J. Cryst. Growth **372**, 15 (2013).

[33] J. J. Hou, N. Han, F. Wang, F. Xiu, S. Yip, A. T. Hui, T. Hung, and J. C. Ho, ACS Nano **6**, 3624 (2012).

[34] C. S. Jung, H. S. Kim, G. B. Jung, K. J. Gong, Y. J. Cho, S. Y. Jang, C. H. Kim, C. W. Lee, and J. Park, J. Phys. Chem. C **115**, 7843 (2011).

[35] Y. Wang, V. Schmidt, S. Senz, and U. Goesele, Nature Nanotechnol. **1**, 186 (2006).

[36] D. E. Perea, J. E. Allen, S. J. May, B. W. Wessels, D. N. Seidman, and L. J. Lauhon, Nano Lett. **6**, 181 (2006).

[37] E. P. A. M. Bakkers, M. T. Borgström, and M. A. Verheijen, MRS Bull. **32**, 117 (2007).

[38] H. Okamoto and T. B. Massalski, Bull. Alloy Phase Diagr. **4**, 190 (1984).

[39] A. Fontcuberta i Morral, C. Colombo, G. Abstreiter, J. Arbiol, and J. R. Morante, Appl. Phys. Lett. **92**, 063112 (2008).

[40] C. Colombo, D. Spirkoska, M. Frimmer, G. Abstreiter, and A. Fontcuberta i Morral, Phys. Rev. B **77**, 155326 (2008).

[41] B. Mandl, J. Stangl, T. Mårtensson, A. Mikkelsen, J. Eriksson, L. S. Karlsson, G. Bauer, L. Samuelson, and W. Seifert, Nano Lett. **6**, 1817 (2006).

[42] S. A. Dayeh, E. T. Yu, and D. Wang, Small **3**, 1683 (2007).

[43] F. Jabeen, V. Grillo, S. Rubini, and F. Martelli, Nanotechnology **19**, 275711 (2008).

[44] J. H. Paek, T. Nishiwaki, M. Yamaguchi, and N. Sawaki, Phys. Status Solidi C **6**, 1436 (2009).

[45] P. Krogstrup, R. Popovitz-Biro, E. Johnson, M. Hannibal Madsen, J. Nygård, and H. Shtrikman, Nano Lett. **10**, 4475 (2010).

[46] G. E. Cirlin, V. G. Dubrovskii, Yu. B. Samsonenko, A. D. Bouravleuv, K. Durose, Y. Y. Proskuryakov, B. Mendes, L. Bowen, M. A. Kaliteevski, R. A. Abram, and D. Zeze, Phys. Rev. B **82**, 035302 (2010).

[47] S. Plissard, G. Larrieu, X. Wallart, and P. Caroff, Nanotechnology **22**, 275602 (2011).

[48] D. Rudolph, S. Hertenberger, S. Bolte, W. Paosangthong, D. Spirkoska, M. Döblinger, M. Bichler, J. J. Finley, G. Abstreiter, and G. Koblmüller, Nano Lett. **11**, 3848 (2011).

[49] D. Rudolph, S. Funk, M. Döblinger, S. Morkötter, S. Hertenberger, L. Schweickert, J. Becker, S. Matich, M. Bichler, D. Spirkoska, I. Zardo, J. J. Finley, G. Abstreiter, and G. Koblmüller, Nano Lett. **13** 1522 (2013).

[50] K. Tomioka, J. Motohisa, S. Hara, and T. Fukui, Nano Lett. **8**, 3475 (2008).

[51] W. Wei, X.-Y. Bao, C. Soci, Y. Ding, Z.-L. Wang, and D. Wang, Nano Lett. **9**, 2926 (2009).

[52] G. Koblmüller, S. Hertenberger, K. Vizbaras, M. Bichler, F. Bao, J.-P. Zhang, and G. Abstreiter, Nanotechnol. **21**, 365602 (2010).

[53] S. Hertenberger, D. Rudolph, S. Bolte, M. Döblinger, M. Bichler, D. Spirkoska, J. J. Finley, G. Abstreiter, and G. Koblmüller, Appl. Phys. Lett. **98**, 123114 (2011).

[54] E. Dimakis, J. Lähnemann, U. Jahn, S. Breuer, M. Hilse, L. Geelhaar, and H. Riechert, Cryst. Growth Des. **11**, 4001 (2011).

[55] M. H. Madsen, M. Aagesen, P. Krogstrup, C. Sörensen, and J. Nygård, Nanoscale Res. Lett. **6**, 516 (2011).

[56] I. Isakov, M. Panfilova, M. J. Sourribes, V. Tileli, A. E. Porter, and P. A. Warburton, Nanotechnology **24**, 985707 (2013).

[57] T. Grap, T. Rieger, Ch. Blömers, T. Schäpers, D. Grützmacher, and M. I. Lepsa, Nanotechnology **24**, 335601 (2013).

[58] M. Heiß, A. Gustafsson, S. Conesa-Boj, F. Peiro, J. R. Morante, G Abstreiter, J. Arbiol, L. Samuelson, and A. Fontcuberta i Morral, Nanotechnology **20**, 075603 (2009).

Phys. Status Solidi RRL **8**, No. 1 (2014)

29

[59] M. Heiß, B. Ketterer, E. Uccelli, J. R. Morante, J. Arbiol, and A. Fontcuberta i Morral, Nanotechnology **22**, 195601 (2011).

[60] K. W. Ng, W. S. Ko, T.-T. D. Tran, R. Chen, M. V. Nazarenko, F. Lu, V. G. Dubrovskii, M. Kamp, A. Forchel, and C. Chang-Hasnain, ACS Nano **7**, 100 (2013).

[61] R. Chen, T.-T. D. Tran, K. W. Ng, W. S. Ko, L. C. Chuang, F. G. Sedgwick, and C. Chang-Hasnain, Nature Photon. **5**, 170 (2011).

[62] L. C. Chuang, R. Chen, F. G. Sedgwick, W. S. Ko, K. W. Ng, T.-T. D. Tran, and C. Chang-Hasnain, Conf. on Lasers and Electro-Optics, May 2010.

[63] J. C. Shin, K. J. Choi, D. Y. Kim, W. J. Choi, and X. Li, Cryst. Growth Design **12**, 2994 (2012).

[64] G. Wulff, Z. Kristallogr. **34**, 449 (1901).

[65] T. Sato, J. Motohisa, J. Noborisaka, S. Hara, T. Fukui, J. Cryst. Growth **310**, 2359 (2008).

[66] T. Sato, Y. Kobayashi, J. Motohisa, S. Hara, T. Fukui, J. Cryst. Growth **310**, 5111 (2008).

[67] M. Yoshimura, K. Tomioka, K. Hiruma, S. Hara, J. Motohisa, T. Fukui, Jpn. J. Appl. Phys. **49**, 04DH08 (2010).

[68] Y. Kohashi, T. Sato, K. Ikejiri, K. Tomioka, S. Hara, and J. Motohisa, J. Cryst. Growth **338**, 47 (2012).

[69] Y. Kohashi, S. Sakita, S. Hara1, and J. Motohis, Appl. Phys. Exp. **6**, 025502 (2013).

[70] S. Hertenberger, Ph.D. thesis, Walter Schottky Institut, Technische Universität München, October 2012, ISBN: 978-3-941650-44-2.

[71] S. Hertenberger, S. Funk, K. Vizbaras, A. Yadav, D. Rudolph, J. Becker, S. Bolte, M. Döblinger, M. Bichler, G. Scarpa, P. Lugli, I. Zardo, J. J. Finley, M.-C. Amann, G. Abstreiter, and G. Koblmüller, Appl. Phys. Lett. **101**, 043116 (2012).

[72] S. Hertenberger, D. Rudolph, M. Bichler, J. J. Finley, G. Abstreiter, and G. Koblmüller, J. Appl. Phys. **108**, 114316 (2010).

[73] S. Hertenberger, D. Rudolph, J. Becker, M. Bichler, J. J. Finley, G. Abstreiter, and G. Koblmüller, Nanotechnology **23**, 235602 (2012).

[74] K. Ikejiri, J. Noborisaka, S. Hara, J. Motohisa, and T. Fukui, J. Cryst. Growth **298**, 616 (2007).

[75] H. Yoshida, K. Ikejiri, T. Sato, S. Hara, K. Hiruma, J. Motohisa, and T. Fukui, J. Cryst. Growth **312**, 52 (2009).

[76] S. Morkötter, S. Funk, M. Liang, M. Döblinger, S. Hertenberger, J. Treu, D. Rudolph, A. Yadav, J. Becker, M. Bichler, G. Scarpa, P. Lugli, I. Zardo, J. J. Finley, G. Abstreiter, and G. Koblmüller, Phys. Rev. B **87**, 205303 (2013).

[77] K. Tomioka, J. Motohisa, S. Hara, and T. Fukui, Jpn. J. Appl. Phys. **46**, L1102 (2007).

[78] D. K. Biegelsen, R. D. Bringans, J. E. Northrup, and L. E. Swartz, Phys. Rev. Lett. **65**, 452 (1990).

[79] T. Hayakawa and M. Morishima, Appl. Phys. Lett **59**, 3321 (1991).

[80] P. Chen, K. C. Rajkumar, and A. Madhukar, Appl. Phys. Lett. **58**, 1771 (1996).

[81] K. Yang and L. J. Schowalter, Appl. Phys. Lett. **60**, 1851 (1992).

[82] J. J. Hou, F. Wang, N. Han, F. Xiu, S. Yip, M. Fang, H. Lin, T. F. Hung, and J. C. Ho, ACS Nano **6**, 9320 (2012).

[83] T. Akiyama, K. Sano, K. Nakamura, and T. Ito, Jpn. J. Appl. Phys. **45**, L245 (2006).

[84] K. A. Dick, J. Bolinsson, M. E. Messing, S. Lehmann, J. Johansson, and P. Caroff, J. Vac. Sci. Technol. B **29**, 04D103 (2011), and references therein.

[85] D. Spirkoska, J. Arbiol, A. Gustafsson, S. Conesa-Boj, F. Glas, I. Zardo, M. Heigoldt, M. H. Gass, A. L. Bleloch, S. Estrade, M. Kaniber, J. Rossler, F. Peiro, J. R. Morante, G. Abstreiter, L. Samuelson, and A. Fontcuberta i Morral, Phys. Rev. B **80**, 245325 (2009).

[86] U. Jahn, J. Lähnemann, C. Pfüller, O. Brandt, S. Breuer, B. Jenichen, M. Ramsteiner, L. Geelhaar, and H. Riechert, Phys. Rev. B **85**, 045323 (2012).

[87] P. Kusch, S. Breuer, M. Ramsteiner, L. Geelhaar, H. Riechert, and S. Reich, Phys. Rev. B **86**, 075317 (2012).

[88] M. Murayama and T. Nakayama, Phys. Rev. B **49**, 4710 (1994).

[89] Z. Zanolli, F. Fuchs, J. Furthmüller, U. von Barth, and F. Bechstedt, Phys. Rev. B **75**, 245121 (2007).

[90] T. B. Hoang, A. F. Moses, H. L. Zhou, D. L. Dheeraj, B. O. Fimland, and H. Weman, Appl. Phys. Lett. **94**, 133105 (2009).

[91] M. Heiss et al., Phys. Rev. B **83**, 045303 (2011).

[92] M. Moewe, L. C. Chuang, S. Crankshaw, C. Chase, and C. Chang-Hasnain, Appl. Phys. Lett. **93**, 023116 (2008).

[93] M. H. Sun, E. S. P. Leong, A. H. Chin, C. Z. Ning, G. E. Cirlin, Y. B. Samsonenko, V. G. Dubrovskii, L. Chuang, and C. Chang-Hasnain, Nanotechnology **21**, 335705 (2010).

[94] J. Trägård, A. I. Persson, J. B. Wagner, D. Hessman, and L. Samuelson, J. Appl. Phys. **101**, 123701 (2007).

[95] G. Koblmüller, K. Vizbaras, S. Hertenberger, S. Bolte, D. Rudolph, J. Becker, M. Döblinger, M.-C. Amann, J. J. Finley, and G. Abstreiter, Appl. Phys. Lett. **101**, 053103 (2012).

[96] C.-Y. Yeh, S.-H. Wei, and A. Zunger, Phys. Rev. B **50**, 2715 (1994).

[97] D. E. Cooper, J. Bajaj, and P. R. Newman, J. Cryst. Growth **86**, 544 (1988).

[98] Y. P. Varshni, Physica **34**, 149 (1967).

[99] I. Vurgaftman, R. J. Meyer, and L. R. Ram-Mohan, J. Appl. Phys. **89**, 5815 (2001).

[100] M. Möller, M. M. Jr. deLima, A. Cantarero, T. Chiaramonte, M. A. Cotta, and F. Iikawa, Nanotechnology **23**, 375704, (2012).

[101] F. Glas, Phys. Rev. B **74**, 121302(R) (2006).

[102] L. C. Chuang, M. Moewe, C. Chase, N. P. Kobayashi, C. Chang-Hasnain, and S. Crankshaw, Appl. Phys. Lett. **90**, 043115 (2007).

[103] K. L. Kavanagh, Semicond. Sci. Technol. **25**, 024006 (2010).

[104] C. P. Svensson, T. Mårtensson, J. Trägårdh, C. Larsson, M. Rask, D. Hessman, L. Samuelson, and J. Ohlsson, Nanotechnology **19**, 305201 (2008).

[105] K. Tomioka, J. Motohisa, S. Hara, K. Hiruma, and T. Fukui, Nano Lett. **10**, 1639 (2010).

[106] R. Chen, T.-T. D. Tran, K. W. Ng, W. S. Ko, L. C. Chuang, F. G. Sedgwick, and C. Chang-Hasnain, Nature Photon. **5**, 170 (2011).

[107] C. Rehnstedt, T. Mårtensson, C. Thelander, L. Samuelson, and L. E. Wernersson, IEEE Trans. Electron. Dev. **55**, 3037 (2008).

[108] T. Tanaka, K. Tomioka, S. Hara, J. Motohisa, E. Sano, and T. Fukui, Appl. Phys. Exp. **3**, 025003 (2010).

[109] W. Wei, X.-Y. Bao, C. Soci, Y. Ding, Z.-L. Wang, and D. Wang, Nano Lett. **9**, 2926 (2009).

[110] J. C. Shin, P. K. Mohseni, K. J. Yu, S. Tomasulo, K. H. Montgomery, M. L. Lee, J. A. Rogers, and X. Li, ACS Nano **6**, 11074 (2012).

[111] L. C. Chuang, F. G. Sedwick, R. Chen, W. S. Ko, M. Moewe, K. W. Ng, T.-T. D. Tran, and C. Chang-Hasnain, Nano Lett. **11**, 385 (2011).

[112] A. C. Seabaugh and Q. Zhang, Proc. IEEE **98**, 2095 (2010).

[113] A. M. Ionescu, and H. Riel, Nature **479**, 329 (2011).

[114] M. T. Björk, H. Schmid, C. D. Bessire, K. E. Moselund, H. Ghoneim, S. Karg, E. Lörtscher, and H. Riel, Appl. Phys. Lett. **97**, 163501 (2010).

[115] K. Tomioka and T. Fukui, Appl. Phys. Lett. **98**, 083114 (2011).

[116] K. E. Moselund, H. Schmid, C. Bessire, M. T. Björk, H. Ghoneim, and H. Riel, IEEE Electron Device Lett. **33**, 1453 (2012).

[117] X. Zhou, E. T. Yu, D. Florescu, J. C. Ramer, D. S. Lee, and E. A. Armour, Appl. Phys. Lett. **85**, 407 (2004).

[118] C. D. Bessire, M. T. Björk, H. Schmid, A. Schenk, K. B. Reuter, and H. Riel, Nano Lett. **11**, 4195 (2011).

[119] A. G. Chynoweth, W. L. Feldmann, and R. A. Logan, Phys. Rev. **121**, 684 (1961).